ISSN 1580-2949
UDK 669+666+678+53 MTAEC9, 41(3)109–154(2007)

MATER. TEHNOL.	LETNIK VOLUME 41	ŠTEV. NO. 3	STR. P. 109–154	LJUBLJANA SLOVENIJA	MAY-JUNE 2007

VSEBINA – CONTENTS

UDC/UDK 669.14.018.298
Review scientific article/Pregledni znanstveni članek

ISSN 1580-2949
MTAEC9, 41(3)111(2007)

STRUCTURAL STEELS WITH MICROMETER GRAIN SIZE: A SURVEY

KONSTRUKCIJSKA JEKLA Z MIKROMETRSKIMI KRISTALNIMI ZRNI: PREGLED

Franc Vodopivec, Dimitrij Kmetič, Franc Tehovnik, Jelena Vojvodič-Tuma

Institute of Metals and Technology, Lepi pot 11, 1000 Ljubljana, Slovenia
franc.vodopivec@imt.si

Prejem rokopisa – received: 2006-11-17; sprejem za objavo – accepted for publication: 2007-03-01

Experimental findings and their theoretical interpretation related to the achieving of a μm grain size in structural steels with a microstructure of ferrite and pearlite are summarised. Several laboratory processing methods can be used to achieve this grain size. It seems that only DIFT (deformation induced ferrite transformation) offers the possibilty of industrial use for thin sheets, while for thicker products DIFT can ensure the small grain size only for a thiN surface layer. By very small grain size yield stress and tensile strength are increased, while elongation, reduction of area and strain hardening are decreased. For a grain size of 1.3 μm upper shelf notch toughness is smaller, toughness transition temperature is lower and lower shelf notch toughness is higher than by the steel with the grain size of 6.8 μm.

Key words: structural steels, ultrafine grain size, processing methods, effect of deformation and temperature, mechanical properties

Predstavljeni in interpretirani so eksperimentalni izsledki raziskovanja s ciljem doseganja mikrometrskih velikosti kristalnih zrn v konstrukcijskih jeklih z mikrostrukturo iz ferita in perlita. Tako velikost zrn je mogoče doseči z več metodami laboratorijskega procesiranja. Po dosedanjih spoznanjih je primerna za industrijsko uporabo za izdelavo tankih trakov le metoda DIFT (deformacijsko inducirana transformacija ferita). Po tej metodi je mogoče pri debelejših ploščah ustvariti zelo majhna zrna samo v tanki plasti ob površini. Pri zelo majhni velikosti zrn se povečata meja plastičnosti in trdnost, zmanjšajo pa se razteznost, kontrakcija in deformacijska utrditev. Pri jeklu z velikostjo zrn 1,3 μm je v območju duktilnega loma zarezna žilavost manjša, prehodna temperatura žilavosti je tudi manjša, žilavost pod to temperaturo pa večja kot pri jeklu z velikostjo zrn 6,8 μm.

Ključne besede: konstrukcijska jekla, zelo majhna kristalna zrna, metode procesiranja, vpliv deformacije in temperature, mehanske lastnosti

1 INTRODUCTION

Yield stress (R_E) increases with decreasing grain size because the grain boundaries hinder the movement of dislocations produced by the cold deformation of metals according to the Hall-Petch equation:

$$R_E = R_o + k \cdot d^{1/2} \quad (1)$$

With: R_o – constant depending on the chemical and phase composition of the steel and k – constant characteristic for the effect of linear grain size (d).

For steels having an essentially ferritic microstructure the following relations were developped for the yield stress and for the notch toughness transition temperature[1]:

$$R_E\ /\text{MPa} = 104.1 + 32.6\ w(\text{Mn}) + 84\ w(\text{Si}) + 17.5\ \text{d}^{-1/2} \quad (2)$$

$$ITT\ /^\circ\text{C} = 19 + 44\ w(\text{Si}) + 700\ w(\text{N}) - 11.5\ d^{-1/2} \quad (3)$$

By smaller grain size the temperature of cleavage of ferrite is lower and the yield stress greater. Other ferrite strengthening mechanisms increase also the temperature of cleavage fracture. For this reason, their exploitation for the increase of yield stress of structural steels is limited. It is predicted[2] that for a steel with a grain size of 5 μm the 50 % fracture appearance transition temperature of –100 °C would decrease to below –200 °C for a grain size of 1 μm. The extent of the beneficial effect of grain size is shown in **Table 1** by comparison of the chemical composition and the share of other of strengthening mechanisms for three structural steels with a microstructure of ferrite and pearlite[3]. The industrial exploitation of the effect of grain size depends on the benefit obtained with the decrease of production costs which may result from the smaller content of alloying elements, the incresed costs of the technology to achieve the aimed grain size rsp. properties and the benefit of the use of the steel with increased yield strength for structures. In the last benefit several costs are included, f.i. lower transportation and erection costs for structures and a smaller quantity of welding consumables. Sometimes, the user can consider as important for the choice of steel also other criteria, f.i. the resistance of the steel to hydrogen embrittlemenst which is of essential importance for steels for vessels for liquid hydrocarbons. It is shown in **Figure 1** than steel C with a grain size of about 3 μm conserves a much greater reduction of area after the NACE test of tensile test after a determined time of maintaninig the specimens at stress level of 80 % of the yield stress in water saturated with H_2S than the

Table 1: Chemical composition and share of strengthening mechanisms for three structural steels
Tabela 1: Kemična sestava in masni delež mehanizmov utrditve za tri konstrucijska jekla

Composition	Element in mass fractions *w*/%								
	C	Mn	Si	Al	Nb	Cr	Ni	Cu	Mo
Steel A	0.21	0.51	0.25	0.027	–	0.02	0.04	0.10	–
Steel B	0.17	1.32	0.32	0.009	–	0.21	0.13	–	–
Steel C	0.08	0.36	0.34	0.052	0.058	0.54	0.27	0.36	0.27
Share of yield stress increase, R_E/MPa									
	SM 1	SM 2	SM 3	Sm 4	Sm 5	SM 6	SM7	YS_{th}	YS_{exp}
Steel A	30	50	17	56	85	–	20	258	265
Steel B	30	61	17	104	135	–	28	372	377
Steel 3	30	15	17	136	254	9	43	504	522

SM 1 – ferrite yield stress, SM 2 – content of pearlite, SM 3 – Interstitial solution, SM 4 – Substitutional solution, SM 5 – Grain size, SM 6 – Dispersion, SM 7 – Precipitation in γ phase, YS_{th} – calculated yield stress, YS_{exp} – Experimental yield stress

steel B with a grain size of about 25 μm inspite the by 1/3 greater yield stress of the first[4]. The fine grained steel in capable to retain in solution and in traps much more hydrogen than the coarse grained steel before the ductility is deteriorated to a significant extent. It is, thus, more resisting to hydrogen embrittlement and also more resistant to the delayed fracture due to the accumulation hydrogen at grain boundaries[2].

Iz is shown later that there are processing routes which have the potential to obtain a grain size of 1 μm in flat products with substatial thickness. These steel will find cost effective applications, but not major markets[5]. The reason is in the fact that the effect different major parameters affecting the grain size, f.i. steel chemistry, relation temperature – deformation intensity, cooling rate and transformation is not knovn to the extent allowing the industrial exploitation or the explotation would require significant investments in the hot working technology, at least for products used for steel structures. Thus, by analysing the potential effect of grain size on structural steels, two aspects should be considered: the scientific and the technological – commercial.

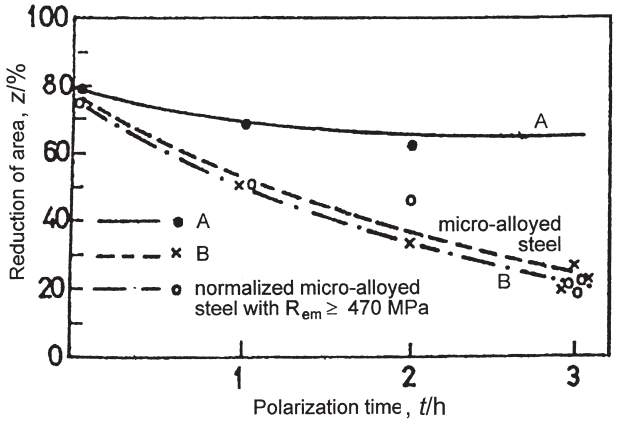

Figure 1: Results of the NACE test for the steels B and C in **Table 1** and a microalloyed normalised steel with yield stress of 470 MPa[4]
Slika 1: Rezultati preizkusa NACE za jekli B in C iz **tabele 1** in za mikrolegirano normalizirano jeklo z mejo plastičnosti 470 MPa[4]

By a given chemical composition, the parameters of hot working of steels of essential importance for the achieving of a small grain size are: the hot working temperature range, the finishing rolling temperature, the per pass deformation and the total plastic deformation in the range of temperature affecting the must the nucleation and the growth of recrystallised grains in deformed austenite or ferrite. One of the problems to overcame is the rate interpass growth of recrystallised grains and the rate of growth of ferrite grains after the austenite to ferrite transformation.

In **Figure 2** the effect of rolling temperature range of 56 mm slabs to 12 mm plates in 6 passes temperature is shown for structural steels with different chemical composition[6,7]. All slabs were soaked at 1250 °C and cooled to a different initial rolling temperature. It is evident, that by several passes rolling the initial size of austenite grains does not affect the grain size in the

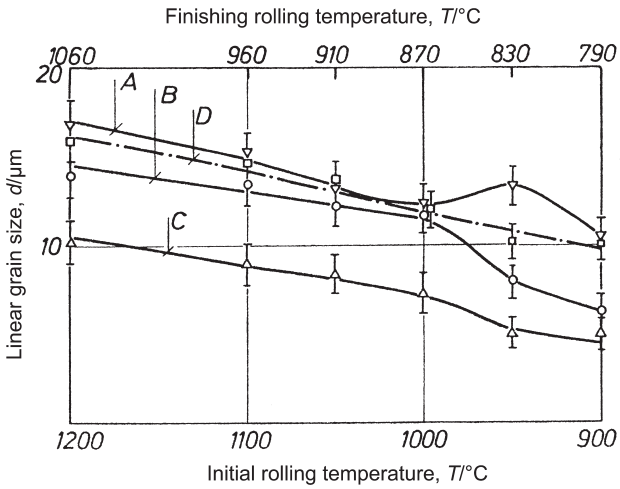

Figure 2: Effect of finishing rolling temperature on linear grain size for several structural steels rolled from 55 mm slabs in 6 passes to 16 mm plates and cooled in air on a warm bed
Slika 2: Vpliv temperature konca valjanja na linearno intercepcijsko dolžino za več konstrukcijskih jekel, ki so bila izvaljana iz 55-milimetrskih slabov v 16-milimetrske plošče v šestih vtikih in ohlajena na zraku na topli podlagi

rolled and air cooled steel. Also, in the applied rolling conditions, the effect of niobium carbide precipitation was very limited, since, only a slightly greater ferrite-pearlite grain size was obtained in steels with similar carbon content and without niobium although the virtually complete precipitation of niobium carbide during the rolling. In **Figure 3** the effect of finishing temperature on grain size is shown for steels with 0.04 % C to 0.13 % C[8]. The rolling regime was virtually identical to that for steels in **Figure 2**. At the same finishing temperature the grain size in the range of 7 μm to 33 μm was obtained. The shape of the curves for different steels on **Figure 3** shows that after a temperature, which depends on the content of carbon, coarser grain size is obtained at lower than by higher finishing rolling temperature. By a finishing temperature of 800 °C the grain size decreases virtually proportionally to the content of carbon in steel (**Figure 4**). From the shape of the relation ship in **Figures 3 and 4** and considering the chemical composition of the steels, it was concluded that the difference between the theoretical transformation temperature of austenite and the real transformation temperature during the rolling was very small and that it depends mostly on the content of carbon in the steel. Also, **Figures 3 and 4** show that the growth of ferrite grains after the last pass (last partial deformation of about 20 %), is very fast. The strong effect of carbon on grain size in as rolled steels is explained with the increasing share of rolling performed in ferrite range

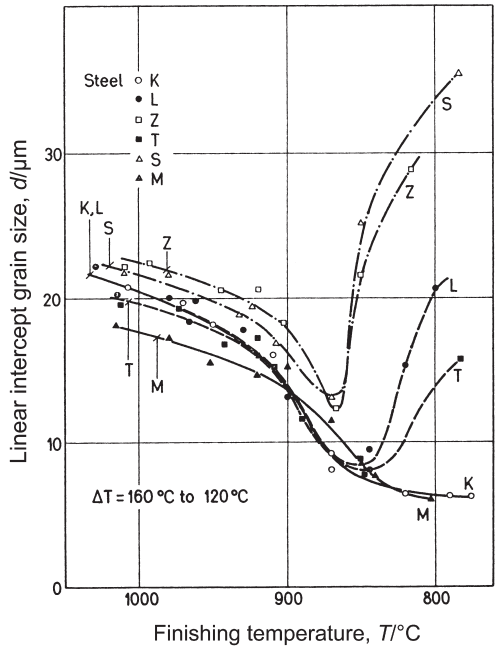

Figure 3: Effect of finishing rolling temperature on the ferrite pearlite grain size for steels with the content of carbon in the range of 0.04 % to 0.13 %. The tests were carried out in the same way as those in **Figure 2**

Slika 3: Vpliv konca temperature valjanja na velikost zrn ferita in perlita za jekla z ogljikom v razponu med 0,04 % in 0,12 %. Preizkusi so bili izvršeni na enak način kot pri jeklih na **sliki 2**

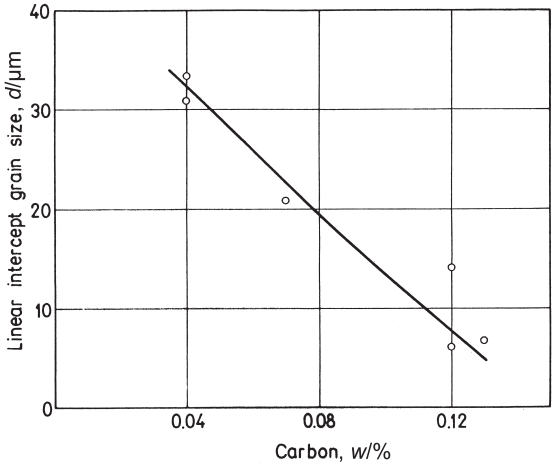

Figure 4: Relationship grain size versus carbon content for steels in **Figure 3** rolled in the temperature range from 900 °C to 790 °C

Slika 4: Velikost zrn v odvisnosti of vsebnosti ogljika za jekla s **slike 3**, ki so bila izvaljana v razponu temperature med 900 °C in 790 °C

with a per pass deformation of approximately 20 %, which is lower than that necessary for the static recrystallisation of this phase, which is of about 60 %[9,10]. According to[11,12] for the static recrystallisation of austenite only a per pass deformation of above 10 % is necessary. In absence of recristallisation, the grain growth of ferrite, termed strain induced coarsening, occurs with a much greater rate than the growth of grains of ferrite produced with the transformation of recrystallised austenite at lower temperature. With the transformation of deformed and non recrystallised grains of austenite in Nb microalloying steel bainite grains of size more than one order of magnitude greater than the size of ferrite and pearlite grains in the surrounding matrix and formed by transformation of recrystallised austenite grains, were obtained, while the transformation of grains of deformed austenite in low carbon steel produced lenticular colonies of coarser, partially acicular ferrite and pearlite grains (**Figure 5**). It is clear, thus,

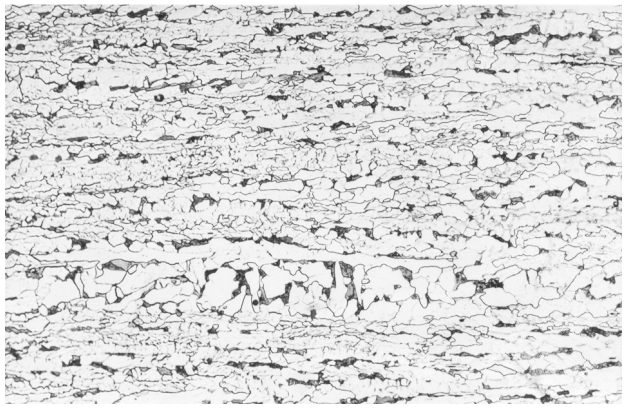

Figure 5: (magn. 200 times) Microstructure of the steel K from **Figure 3** rolled in the temperature range from 900 °C to 774 °C

Slika 5: (pov. 200-kratna) Mikrostruktura jekla K s **slike 3**, ki je bilo izvaljano v razponu temperature od 900 °C do 774 °C

that the achievement of μm and smaller size of ferrite grains in structural steels is a problem of rolling technology, and for a given chemical composition of the steel, it depends on the deformation and the temperature of final rolling passes, the austenite to ferrite transformation temperature and the cooling of the rolled steel. It is usefull to remember that the general tendency in the development of modern structural steeels is assotiated with a constant lowering of the content of carbon[13], as shown in **Figure 6**.

In this survey the parameters related to the grain size of structural steels will be discussed considering the tests aimed to determine what can be achieved in laboratory and is, in this moment and in the near future, outside the potential of the present technology and what may be achieved with acceptable changes of the present technology.

2 THEORETICAL ROUTES TO ACHIEVE A SMALL GRAIN SIZE

The benefit of grain size is achieved with small crystal grains with high angle boundaries able to stop moving dislocations produced by cold deformation by testing of tensile properties at room temperature. High angle boundaries are achieved with recrystallisation of austenite and ferrite, mostly static, and with the austenite to ferrite transformation. It is, thus, logical to assume, than small grain size involving the phase transformation can be obtained only from austenite with very small grain size and the prevention of ferrite grain growth. If the small grain size is to be obtained with static recrystallisation of ferrite at hot rolling, a very great plastic deformation is necessary, in one pass or in several passes on condition of incomplete per pass relaxation of deformation energy.

The recrystallisatuon behaviour of austenite depends on the steel chemistry. For the calculations of the temperature of the end of static recrystallisation of austenite the following equation was deduced for the effect of different alloying elements in wt %[14]:

$$T_{nr} = 887 + 464\ w(C) + 890\ w(Ti) - 357\ w(Si) + \\ + 6445\ w(Nb) - 644\ w(Nb)^{1/2} + 363\ w(Al) \quad (3)$$

The effect of nobium is the greater and it is related to the precipitation of niobium carbide (NbC). For the calculation of the temperature of precipitation of this carbide the following relation was proposed[14]:

$$T_{NbC}/°C = -6770/\{\lg\ [w(Nb) \times w(C)] - 2.26\} - 273 \quad (4)$$

The rate of precipitation of NbC is at the same temperature for approximately three orders of magnitude greater during the deformation of austenite and for two orders of magnitude greater in deformed austenite[15,16] than in recrystallised austenite and the increase of strain rate lowers the recrystallisation and the precipitation temperature[17]. The explanation of the delaying effect of niobium is that strain induced precipitates hinder the growth recrystallisation nuclea from reaching the critical size required for their growth in deformed austenite. Within this explanation it is not clear why the effect of titatium is smaller than that of niobium. By equal weight content, the atomic content of titanium is greater and the solubility product for titanium carbide is even smaller than that for NbC. For this reason, a similar effect of titanium would be expected even at higher temperature than that of niobium. It is interesting to note, with respect to the mechanism of the effect of niobium on recystallisation of austenite, that it was found with dilatometric investigations of recrystallitaion and precipitation, that niobium in solid solution in ferrite delayed the recrystallisation of this phase[14]. Other alloying elements have a much smaller effect of the temperature of static recrystallisation of austenite and, for this reason, can not be, exploited for the achieving of small grain size. In all cases, the presence of a determined number of precipitates is necessary to prevent the growth of recrystallised austenite and ferrite grains.

The microstructure of fine grained structural steels consists of ferrite, pearlite and bainite in different combinations and can be achieved with the trasformation of fine grained austenite. For a given steel chemistry, the austenite grain size depends on the extent of deformation and the growth of recrystallised grain in interpass time, the time of cooling below the minimal grain growth temperature or the time to the transformation to ferrite. It was found that, indepenedently on the cooling rate, after holding of the deformed austenite for 100 s at 900 °C, the steel had a ferrite grain size 1 μm greater than without holding time[14]. The explanation was in the rapid coarsening of NbC precipitates.

In laboratory, it is possible to vary in a large range all the parameters affecting the grain size. At this time, the smallest grain size is achieved with ECAP[18] (equal channel angular pressing) or hot pressing. The deformation energy is dispersed motly as heat, for this reason, test with great deformation or deformation rate are not isothermal. The rate of plastic deformation is generally

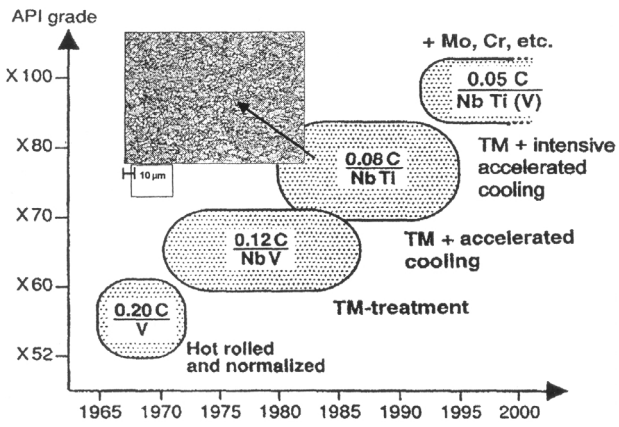

Figure 6: Evolutionary trend for high strength steels for linepipes
Slika 6: Smer evolucije visokotrdnih jekel za cevi

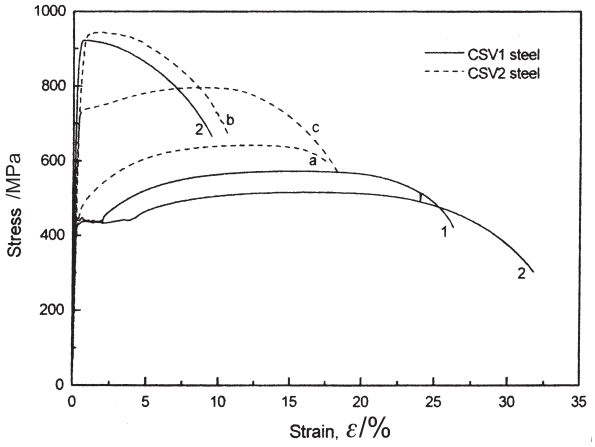

Figure 7: Stress-strain curves for two steels before V(1) and after ECAP V(2)

Slika 7: Odvisnosti napetost-deformacija za dve jekli pred ECAP V(1) in po njem V(2)

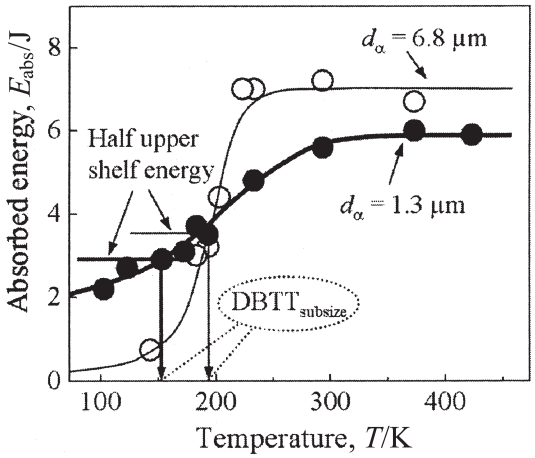

Figure 8: Effect of test temperature on absorbed energy for two steels with grain size 6.8 μm and 1.3 μm

Slika 8: Vpliv temperature preizkusa na energijo preloma za dve jekli z velikostjo zrn 6,8 μm in 1,3 μm

high and, for this reason, the deformation energy may be generated adiabatically and the steel in the deformation zone heated significantly above the nominal deformation temperature.

With ECAP processing[18] a grain size below 1 μm can be obtained with interstitial free steels. With 4 passes of ECAP at 623 K a ferrite grain size of 0.3 μm and severely deformed pearlitic cementite were achieved in a steel with 0.15 % C, 0.25 % Si and 1.1 % Mn and the initial intercept length of ~ 30 μm. The yield stress was increased from 300 MPa to 944 MPa, while, the ductility was decreased to less than one half of the initial level. The addition of 0.06 % V to the steel had no visible effect on the properties after ECAP inspite of the fact, that the initial grain size was of ~ 10 μm, thus only 1/3 of that in the case of the vanadium free steel. The increase of ECAP passes from 4 to 8 did not affect the grain size and the yield stress, it increased however the misorientation of the grain boundaries[19,20]. The conclusions were that that by multiple ECAP the effect of initial grain size is not significant.

The tensile properties were changed significantly after ECAP deformation of the 0.15 % C, 0.25 % Si, 1.12 % Mn, 0.34 % V and 0.012 % N, yield stress was increased from 435 MPa to 920 MPa, tensile strength for 568 MPa to 920 MPa, uniform elongation was decreased from 17 % to 2 % and total elongation from 28 % to 9 % (**Figure 7**)[21]. If during the ECAP test nanosize precipitation of vanadium carbide occured, the precipitates improved the thermal stability of nanostructure and of tensile properties of the steel, while, the particles obtained with normalisation before ECAP had no significant effect of the thermal stability of the ECAP nanostructure[21].

With ECAP at 500 °C and intercritical annealing of the 0.15 % C,0.25 % Si and 1.1 % Mn the achieved grain size of ferrite grains and martensite islands was of 0.8 μm[22], the yield stress, of 540 MPa, tensile stregth of 890 MPa, uniform elongation of 9.8 % and total elongatiopn of 17.6 %. By difference of results achieved with other types of steel, the investigated steel exibited an extensive strain hardening.

With four pass compression with a total strain of ε = 1.6 in the temperature range from 1143 °C to 823 °C the grains size of a 0.22 % C and 0.74 % Mn steel was diminished from 6.8 μm to 1.3 μm, yield stress increased from 360 MPa to 540 MPa[23] and the elongation was decreased from 31 % to 16 %. This decrease was explained in terms of smaller strain hardening due to the spreading of dislocation in the grain boundaries of ferrite grains. Of special interest in the finding that by small grain size the upper shelf absorbed energy was smaller than by coarse grain size, while the transition temperature was lower and the transition range was greater (**Figure 8**). The greater notch toughness below the value of half upper shelf energy was explained in terms of delamination occurring at the fracturing in lower temperature range, which may be related to a stronger texture of crystal grains in the fracture plane.

The one pass hot pressing eliminates the changes of micro/nano structure during the interpass time, avoids the multi axial deformation and enables the analysis of the micro/nano structure obtained at different strain level[24]. The transformation grain refinement (TGR) and recrystallisation grain refinement (RGR) are suggested as potential routes to achieve μm grain size. Both routes can be carried out f.i., with tests of ECAP, hot pressing or warm rolling. By one pass pressing of 0.16 % C, 0.41 % Si and 1.43 % Mn at 823 °C and 10^{-1}s they were able to distinguish the different steps of the formation of small grains. First the original grain are compressed and elongated in the direction of metal flow and low angle boundaries are introduced because of the parallel rotation of elongated grains. At the strain of 2.5 fine equiaxed grains appear at high angle boundaries of initial

grains, at the strain of 4 the share of fine new grains is significant and it increases continously with the increasing plastic deformation. The formation of these grains is explained with work hardening accompanied with grain subdivision and dynamical recovery occuring simultateusly at warm working temperatures. With warm pressing deformation in four passes with the per pas deformation of of $\varepsilon = 0.4$ in temperatrure range from 600 °C to 710 °C in a 0.36 % C, 0.53 % Mn, 0.22 % Si equiaxed ferrite grains of size 1 μm to 2 μm and an uniform distribution of even smaller cementite particles were attained[25].

The different routes to achieve small grain size are discussed also in[26] where also experimental work was performed with the aim to verify the exploitation of the deformation induced ferrrite transformation (DIFT) and the accumulative roll bonding. The investigation was performed in the frame of a ECSC project aimed to identify whether ultrafine grained steels were a potential commercial opportunity or just an academic curiosity. It was established that deformation induced ferrite transformation (DIFT) occurs at a critical strain, which is related to the chemistry of the steel and that carbon in solution in austenite increases the critical strain and retards the DIFT.

The process of DIFT consists of rolling a coarse grained steel close to the Ar_1 level with a reduction of 30–40 %[27]. The undecooling due to the roll chilling and the high shear strain at the sheet surface, increases greatly the nucleation rate in austenite grains. In this way, a very rapid austenite transformation is achieved over the whole austenite grain. It seems that the strain enegy of deformed austenite may induce the transformation to ferrite slightly above the Ar_3 point[28,29,30], in agreement with **Figure 3**.

In the thermodinamic analyis of DIFT[31] it is assumed that the deformation elongates austenite grains, increases the grain boundary area and enhances the disorder of the grain boundary structure and the grain boundary energy per unit area. Analytical relations were developped to calculate the increase of free energy in dependence of the deformation degree and rate. Two nucleation sites for the transformation induced ferrite (DIF) were observed: austenite grain boundaries and two sites in the interior of austenite grains: deformation bands and the new formed γ/α interface. The share of DIFT in the steels increases strongly with the deformation and it is of approximately 25 % by a strain of 0.4 and of 80 % by a strain of 1.2. With laboratory DIFT rolling of a 0.09 %C, 0.47 %Si, 1.38 %Mn, 0.1 %V, 0.04 %Nb, 0.02 %Al and 0.018 %N steel in the temperature range of 1473 K to1093 K with a strain of 0.93 at the final thre passes grain size of 1.5 μm was obtained.

With DIFT in a microalloyed structural low carbon steel[32] (X65 steel) a grain size of 1.22 μm and the volume share of DIFT ferrite of 71 % were obtained by the hot rolling reduction of 69 %, the grain size of 0.92 μm and a volume share of DIFT ferrite of 98 % were obtained after a deformation of 88 %. The precipitation of niobium should occurr before the final rolling passes. If not achieved, coarser grain size, similar to that in **Figure 5**, is obtained after air cooling.

The 0.08 %C, 1,74 %Mn and 0.18 %Ti steel was rolled rolled in 6 passes from 30 mm to 5 mm with the finishing temperature in the range 790 °C to 820 °C and cooled with the rate in the range od 20 °C/s to 40 °C/s to the coiling temperature of 550 °C[33]. A microstructure consisting of ferrite of average linear size of approximately 1.5 μm by a cooling velocity of 20 °C/s and bainite by a cooling rate of 30 °C/s were obtained. With the microstructure of ferrite the yield stress of 500 MPa and the elongation of 27 % were obtained, while with a microstructure of 90 % of bainite the yield stress was of 835 MPa and the elongation of 20 %.

The ferrite grain size of approximately 2 μm seems to be the minimal size, which can be abtained by he DIFT mechanims and heavy rolling deformation of supercooled austenite using the existing rolling facilities[34]. Further refining doesn't seems to improve the mechanical properties as compared to the effects to be made. In this reference three temperature (T_d) domains of grain refinenement by heavy deformation are mentioned. Deformation of supercooled austenite ($T_d > Ar_3$) and DIFT refinement mechanism and limit grain size of 2 μm, deformation of a duplex austenite + ferrite initial microstructure ($Ar_3 > T_d > A_{r1}$) and refining by DIFT or DRX (dynamic recrystallisation of ferrite) and limit grain size of 1 μm and deformation of ferrite ($T_d < Ar_1$) with the limit grain size of 0.6 μm. Ferrite grain size obtained with dynamic transformation is finer than that obtained with static recrystallisation. No data on the extent of deformation are given in this reference.

3 CONCLUSION

Micrometer grain size can be obtained for low carbon structural steels with several methods. Virtually all of them are suited for laboratory processing, only DIFT (deformation induced ferrite transformation) and low temperature transformation of recrystallised austenite seems to offer the industrial feasibility. Several authors confirm that by μm grain size yield stress and tensile strength are greatly increased, while and elongation is significantly decreased. In one reference it was found, that by the upper shelf ductile fracturing energy was lower for the same steel by the 1.3 μm than by the 6.8 μm grain size. On the contrary below the temperature of half of the maximal fracture energy, the toughness was greater for the steel with smaller grain size.

The DIFT processing seems to be suited for the production of thin sheets, for thicker product the μm size of grains can be obtained only in a relatively this surface layer. For thicker plates, a small grain size can be achieved with strictly controlled termomechanical

rolling involving the completed recrystallisation of plastically deformed austenite, it transformation to polygonal ferrite at a low temperature, and a sufficiently rapid cooling to prevent the ferrite grain growth. For such processing only niobium microalloyed steel are suited. The chemical composition of the steel should ensure a low temperature of precipitation of niobium carbide and and a low transformation temperature of recrystallised austenite to polygonal ferrite.

4 REFERENCES

[1] F. B. Pickering, T. Gladman: Metallurgical Development in carbon steels; ISI, 1963, 10–20

[2] Ultra Steels for the 21st Century; Center for Structural Materials Research, National Institute for Materials Research, Japan, 2001

[3] F. Vodopivec, J. Vojvodič - Tuma, M. Lovrečič - Saražin: Kovine Zlit. Tehnol. 32 (**1998**), 463

[4] S. Ažman, L. Vehovar, J. Vojvodič-Tuma: Razvoj čelika mikrolegiranog niobijem i molibdenom (Development of a steel microalloyed with niobium and molybdenum), Zavarivanje 96, Beograd, 58–60

[5] J. A. A. Hove: Mat. Sci. Techn. 16 (**2000**), 1264

[6] F. Vodopivec, M. Gabrovšek, J. Žvokelj: Želez. zb. 17 (**1985**),17

[7] A. Preloščan, F. Vodopivec, I. Mamuzić: Mater. tehnol. 36 (**2002**), 181

[8] F. Vodopivec, M. Gabrovšek, J. Žvokelj: Transactions ISIJ 28 (**1988**) 117

[9] D. N. Hawkins: Metals Techn. 5 (**1978**), 37

[10] S. Gohda, T. Watanebe, J. Hashimoto: Trans. ISIJ 21 (**1981**), 6

[11] T. Tanaka, N. Tabata, T. Hatamura, C. Shiga: Microalloying 75, UCC Corpor., Nery York, 1975, 107

[12] I. Kozasu, C. Ouchi, T. Sampei, T. Okita: Microlloying 75, UCC Corpor., New York, 1975, 120

[13] G. Buzzichelli, E. Anelli: ISIJ Intern. 42 (**2002**), 1354

[14] C. Mesplont: Grain refinement and high precipitation hardening by combining microalloying and ultra fast cooling; Proceedings of the 1th International Conference on super – high strength steels, Rome, Italy, 2–4 Nov. 2005

[15] I. Weiss, J. J. Jonas: Metall. Trans. 11 A (**1980**), 403

[16] J. J. Jonas, I. Weiss: Met. Sci. 3 (**1979**), 238

[17] S. F. Medina, A. Quispe: Mat. Sci. Techn 16 (**2000**), 635

[18] Z. Horita, M. Furukawa, M. Nemoto, T. G.Langdon: Mat. Sci. Techn. 16 (**2000**), 1239

[19] D. H. Shin, J. J. Park, S.Y Chang, Y. K. Lee, K. T. Park: ISIJ Intern. 42 (**2002**), 1490

[20] D. H. Shin, W. G. Kim, J. Y Ahn, K. T. Park, N. J. Kim: Fabrication and tensile properties of ultrafine grained steels; Proceedings of the 1th International Conference on super – high strength steels, Rome, Italy, 2–4 Nov., 2005

[21] K. T. Park, S. Y Han, D. H. Shin, Y. K. Lee, K. S. Lee: ISIJ Intern. 4 (**2006**), 1057

[22] K. T. Park, Y. K. Lee, D. H. Shin: I/SIJ Intern. 45 (**2005**) 9, 750

[23] R. Song, D. Ponge, D. Raabe: Mechanical properties of an ultrafine grained C-Mn steel; Proceedings of the 1th International Conference on super – high strength steels, Rome, Italy, 2–4 Nov., 2005

[24] S. V. S. Narayama Murty, S. Torizuka, K. Nagai: ISIJ Intern. 45 (**2005**), 1651

[25] L. Sorojeva, R. Kaspar, D. Ponge: ISIJ Intern. 44 (**2004**), 1211

[26] I. Salvatori: Ultrafine grained steels by advanced thermomechanical processes and severe plastic deformation; Proceedings of the 1th International Conference on super – high strength steels, Rome, Italy, 2–4 Nov., 2005

[27] P. J. Hurley, B. C. Module, P. D. Hogson in Thermomechanical Processing of steels 2000, London, Mai 2000, 476 (loc. cit. ref. 24)

[28] M. R. Higson, P. D. Hogson: Mater. Sci. Technol. 15 (**2000**), 85

[29] J. K. Choi, D. H. Seo, K. Umk, W. Y. Choo: ISIJ Intern. 43 (**2003**), 764

[30] S.C. Hong, S. H. Lim, H. S. Hong, K. J. Lee, D. H. Shin, K. S Lee: Mat. Sci. Techn. 20 (**2004**), 207

[31] X. Sun, Q. Liu, H. Dong: Deformation induced ferrite transformation and grain refinement in low carbon steel; Proceedings of the 1th International conference on Super – high strength steels, Rome, Italy, 2–4 Nov. 2005

[32] H. Dong, Y. Gan,Y. Weng: Research activities on advanced steels in Nercast; Proceedings of the 1th International conference on Super – high strength steels, Rome, Italy, 2–4 Nov., 2005

[33] J. K. Choi: Development of high strength and high performance steels at Posco through Hipers-21 project; Proceedings of the 1th International conference on Super – high strength steels, Rome, Italy, 2–4 Nov. 2005

[34] H. L. Yi, L. X. Du, G. D. Wang, X. H. Liu: ISJ Intern. 46 (**2006**), 754

UDC/UDK 621.77.014:519.68
Original scientific article/Izvirni znanstveni članek

ISSN 1580-2949
MTAEC9, 41(3)119(2007)

THE IMPLEMENTATION OF AN ONLINE MATHEMATICAL MODEL OF BILLET REHEATING IN AN OFU FURNACE

IMPLEMENTACIJA SIMULACIJSKEGA MODELA ZA SPREMLJANJE OGREVANJA GREDIC V OFU-PEČI

Anton Jaklič[1], Franci Vode[1], Tomaž Marolt[2], Boris Kumer[2]

[1]Inštitut za kovinske materiale in tehnologije, Lepi pot 11, 1000 Ljubljana, Slovenia
[2]Štore Steel, d. o. o., Železarska cesta 3, 3220 Štore, Slovenia
anton.jaklic@imt.si

Prejem rokopisa – received: 2007-01-15; sprejem za objavo – accepted for publication: 2007-03-29

We present the implementation of an online mathematical model for billet reheating in the OFU walking-beam furnace at the Štore Steel d.o.o. steelworks in Slovenia. For the real-time operation of the simulation model the data about furnace charging and real-time measurements in the furnace are needed. The simulation model is connected to the existing information system of the OFU furnace, which can ensure the required data. The simulation is performed for all the billets (up to 125) that are currently charged in the furnace. The modeling of the reheating process in a gas-fired walking-beam furnace consists of descriptions of complex partial mechanisms. For the validation of the model, measurements of the billet reheating in the OFU furnace were made. These measurements involved a test billet and five trailing thermocouples. The comparison of the measurements and the simulation results, which are stored in a local database, shows good agreement across the whole temperature range of the reheating process. For a user-friendly presentation of the simulation-model results we developed a graphical user interface. This GUI allows the selection of particular billet from a visualization on the screen of the billets in the furnace. The temperature field and the history of reheating for individual positions of the billet in the furnace are shown for the selected billet. The system has been used online in the production process since May 2006.

Key words: simulation of reheating, billet reheating, real-time simulation, reheating furnace, walking-beam furnace

V prispevku je opisana implementacija simulacijskega modela za spremljanje ogrevanja gredic v OFU-peči v valjarni Štore-Steel, d. o. o. Simulacijski model za delovanje v realnem času potrebuje podatke o trenutnih meritvah temperatur con peči in podatke o založitvi peči, zato je povezan na obstoječ informacijski sistem OFU-peči. Simulacija se izvaja v realnem času za vse gredice, ki so založene v peči (do 125). Modeliranje ogrevnega procesa v plinsko ogrevani koračni peči je sestavljeno iz obravnave kompleksnih delnih mehanizmov. Vrednotenje simulacijskega modela je bilo izvedeno z meritvami ogrevanja gredice v OFU peči. Meritve ogrevanja so bile izvedene med proizvodnim procesom na preizkusni gredici s petimi vlečnimi termoelementi hkrati. Primerjava izračuna in meritev kaže dobro ujemanje v celotnem poteku ogrevanja. Rezultati simulacije se shranjujejo v lokalno bazo podatkov. Za uporabniško prijazen prikaz rezultatov simulacije je bil razvit grafični uporabniški vmesnik. Ta omogoča izbiro poljubne gredice med prikazanimi gredicami, ki so založene v peči. Za izbrano gredico se prikaže trenutno temperaturno polje in celotna zgodovina ogrevanja po posameznih položajih v peči. Sistem se v rednem proizvodnem procesu uporablja od maja 2006.

Ključne besede: simulacija ogrevanja, ogrevanje gredic, simulacija v realnem času, ogrevna peč, koračna peč

1 INTRODUCTION

A computer-controlled hot-rolling process for steel billets requires high-quality reheated billets in terms of time, temperature, thermal profile and furnace atmosphere. When the furnace operates in steady-state conditions the reheating history of every billet is very similar; this type of operation can normally not be achieved. During the normal, non-steady-state, production process various transient operating conditions occur in the furnace : planned and unplanned stoppages in the mill's operation, changing steel grades with varying drop-out temperatures and different thermodynamic properties, changing the stock dimensions, etc. During this kind of transient operation every billet is reheated under different reheating conditions. Therefore, the reheating history of almost every billet is different. For transient-type furnace operation information about the temperature field for all (up to 125) billets in the furnace is very important for successful furnace control and operation. Unfortunately, however, existing measuring methods cannot provide the temperature fields of billets in the furnace. Nevertheless, by using trailing thermocouples it is possible to measure the reheating at a few measuring points inside the test billet. By contrast, measurements using optical pyrometers or thermal cameras in the furnace only give information about the surface temperature of the billets. The use of an online simulation model is the most appropriate way to acquire the real-time temperature fields of billets in the furnace.

In the Štore Steel, d. o. o. steelworks a continuous walking-beam furnace (**Figure 1**) is used for the reheating of steel billets. The furnace has three control zones. The material flow through the furnace is discontinuous, with fixed walking-beam steps. The furnace has 125 billet positions; however, it is possible to charge only every second or every third walking-beam

a

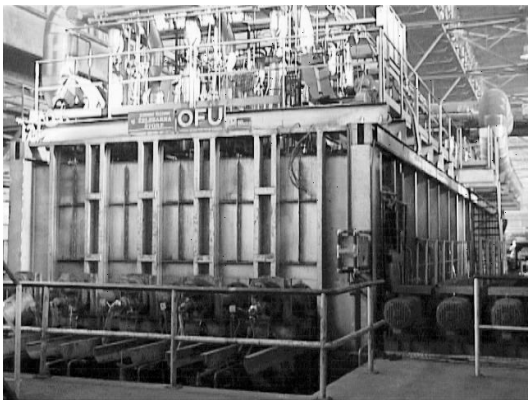

b

Figure 1: a) OFU walking-beam furnace, b) billets in the furnace
Slika 1: a) OFU-koračna peč za ogrevanje gredic, b) gredice v peči

step in order to shorten the residing time of the billets in the furnace.

In recent years, simulation models of reheating furnaces that calculate the actual temperature distribution in the stock have been developed with increasing computational power. The current state of the art are one- or two-dimensional calculations of the stock temperature [1,2,3,4]. However, the first attempts were made to calculate the stock temperature in three dimensions [5,6,7] for different types of reheating furnaces, but not in real-time. A 3D online simulation model of reheating in a walking-beam furnace is presented in [8]. The implementation of an online simulation model in a pusher-type furnace is presented in [9].

In this paper we present the implementation of the 3D online simulation model of the OFU walking-beam furnace.

2 EXPERIMENTAL WORK

The implementation of the simulation model for the online operation of the furnace includes the development of modules to provide real-time measuring data from the furnace, to provide and recognize the current furnace charge, to provide the thermal properties of different steel grades, to store the simulation results in a database, and to present the simulation results in a user-friendly form.

2.1 Mathematical model

The online mathematical model used in the implementation is presented in detail in [8,10]. The determination of the temperature fields of the billets is based on algorithms that include the main physical phenomena associated with the reheating process in a natural-gas-fired walking-beam furnace. Thermal radiation represents the dominant contribution of heat transfer in a high-temperature reheating furnace. The heat exchange between the furnace gas, the furnace wall and the billet surface is calculated using the three-temperature model of Heiligenstaedt.[11] Heat radiation between the surfaces inside the furnace (the furnace-wall surfaces and the billet surfaces) is described using a view-factor matrix. This matrix is obtained before the simulation using the Monte Carlo method. The heat conduction in the billets is calculated using a 3D finite-difference method. The algorithms in the model are optimized to allow a real-time simulation.

2.2 Obtaining the real-time data

For the online operation of the simulation model the real-time data of furnace charging and furnace measurements are needed. The simulation model is connected to the existing furnace-process computer of the OFU furnace (**Figure 2**), which provides the real-time data about furnace-charging measurements in the furnace. Both computers are connected by an Ethernet connection. The data transfer is performed with ASCII files using file-transfer protocol (FTP).

A data file "OFU.DAT" is generated every 30 s by the OFU furnace-process computer. It contains both online measurement data and charging data. The measurement data include:

- Date and time of the measurements
- Temperature measurements of the three control zones
- The gas/air flows of individual control zones
- Oxygen measurements
- Pressure measurements
- Measurements of the recuperator temperatures.

The charging data are written in table form and include information about current positions and other important information about the billets in the furnace. The data for an individual billet in the table consist of:

- Billet position
- Working order
- Serial number of the billet in the working order
- Steel grade
- Billet dimensions
- Date and time of charging

The "OFU.DAT" file is transferred from the furnace-process computer to a computer with the simulation model at regular intervals (i.e., every 20 s) by the process "ftp-transfer", which runs on the computer with the simulation model. After the transfer the file is

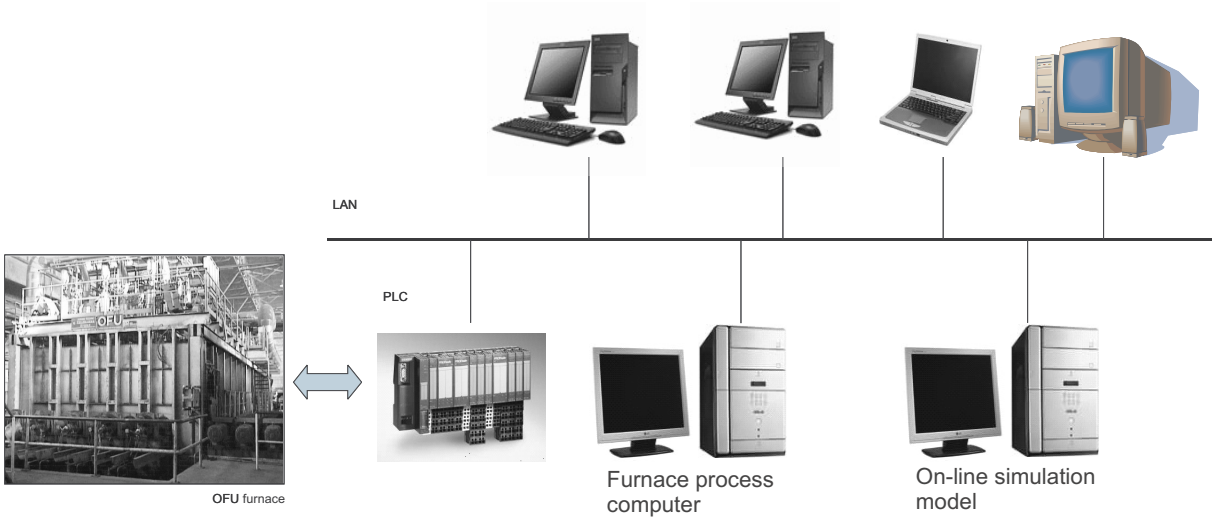

Figure 2: The connection of the simulation model to the OFU furnace-process computer
Slika 2: Povezava simulacijskega modela s procesnim računalnikom OFU peči

deleted on the main process computer. The intervals for transferring the data file have to be shorter than the intervals for writing the data to the file to prevent data loss.

2.3 Thermal properties data

The thermal properties (the specific heat and the heat conduction) of steel billets have a significant influence on the reheating process. Generally speaking, these properties are temperature dependent. In the model the tables are written in ASCII files. In the production process different steel grades with different thermal properties are reheated in the furnace; however, some of them have similar thermal properties. Therefore, all types of steel grades are classified into main groups, and for these groups the thermal properties were measured or obtained from the literature. The automatic classification is based on a uniform classification table, where the corresponding steel group is written for each steel grade in the table. When the billet is added to the charging list the corresponding steel group is recognized on the basis of the steel billet's grade. The system then reads from the files the temperature-dependant specific heat and the heat-conduction tables for the recognized steel group. These data are used for the calculation of the thermal conduction inside the billet.

2.4 Automatic recognition of the charging events

The system is capable of automatic recognition of the charging events and the charging interventions of the furnace operator on the basis of a comparison between the billet-charging table and the charging file. At the end of the event-recognition process the charging table and charging file have to be harmonized. The recognition of charging events is a three-stage process.

In the first stage every billet in the charging table is tested to see if it is present in the charging file. The billets that are absent are deleted from the charging table; their reheating history is saved in the archive directory.

In the second stage every billet in the charging file is tested to see if it is on the charging list. The billets that are absent are added to the charging list and a new file with billet data is opened and filled with the initial data.

After the first and second stages we can be sure that the same billets are included in the charging list and in the charging file. In the third stage the billets in the charging list are sorted into the same order as in the charging file. The position of every billet in the charging list is compared to that in the charging file. If the position is different, then the position in the list is changed and the current calculated temperature field and the position data are written in the reheating file of that billet. The same algorithm is used for single and for double charging and also for transitional operations: single-to-double and double-to-single charging.

2.5 Database structure

All the results of the simulation model are stored in a local database named "**ofu**" (**Figure 3**). The system uses the open-source database system MySQL. The database can be accessed locally by the online simulation model and the human-machine interface (HMI) or through an Ethernet connection by PC workstations in the local area network (LAN).

The database consists of data tables. At every simulation step (30 seconds) the simulation model creates the data table "ofu_online" (**Figure 3**). The records in the table correspond to the billets in the furnace. Each record in the table includes basic billet data (Working order, Serial number in the working

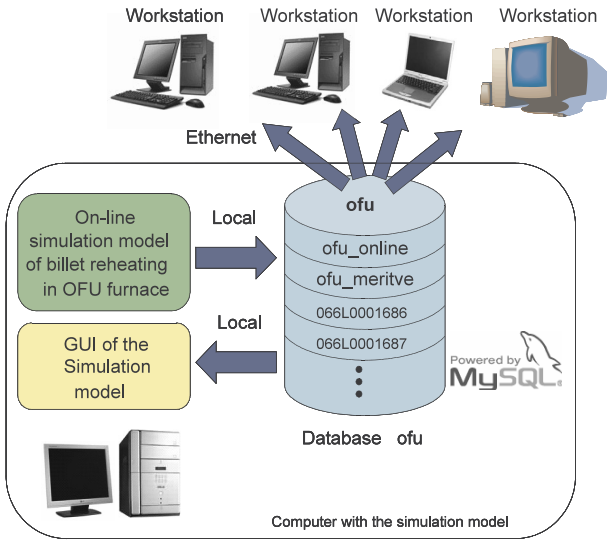

Figure 3: Database structure and availability
Slika 3: Struktura in dostopnost baze podatkov

order, Steel grade, Billet width, Billet height, Billet length, Charging time, Real-time of last calculation, Number of the walking-beam step, Position in the furnace, Residing time at the position, Residing time in furnace) and the characteristic points of the last-calculated temperature field of the billet (**Figure 4**).

In cases when the charging situation in the furnace is changed (new billet charged, billet discharged, walking-beam step) the simulation model writes changes into the "Working order tables" (the names of the tables are working-order names, i.e., "066L0001686"). For those billets for which the position is changed the model writes the record of the last calculated temperature field into the table with the name that corresponds to the billet working order. The record has the same fields as the record for the table "ofu_online". Therefore, the "Working order tables" include the position-dependent history of reheating in the furnace for all the billets of the working order.

When new measurements from the furnace are available (every 30 seconds) the simulation model adds

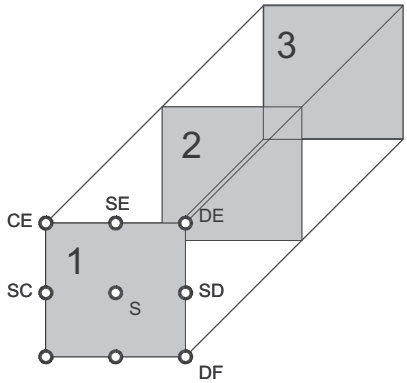

Figure 4: Characteristic points on the billet cross-sections
Slika 4: Karakteristične točke na prerezih gredice

the record with the measurement data to the data table "ofu_meritve" (**Figure 3**). The record consists of the following: Time of measurement, Temperature zone 1, Temperature zone 2, Temperature zone 3, Fuel-consumption zone 1, Air-consumption zone 1, Fuel-consumption zone 2, Air-consumption zone 2, Fuel-consumption zone 3, Air-consumption zone 3, Furnace pressure, Oxygen probe 1, Oxygen probe 2, Oxygen probe 3, Combustion-air temperature, Waste-gas temperature before recuperator, Waste-gas temperature after recuperator.

2.6 Human-machine interface

The human-machine interface (HMI) (**Figure 5**) was developed for the user-friendly presentation of the real-time results of the simulation model. The HMI process runs parallel to the simulation model. The HMI gets all the data from the "ofu" database. There are two modes of HMI operation: real-time and archive.

When the HMI runs in real-time mode the top view of the furnace containing charged billets is shown in the upper part of the window (**Figure 5**). The billet is selected with a mouse click. In the lower part of the window are detailed data about the selected billet: Working order, serial number, steel grade, dimensions, etc. The calculated temperatures of the characteristic points on the cross-section are presented numerically and using a thermal scale. Different diagram presentations, such as the reheating temperatures of three selected points in the billet, the temperatures of individual furnace-control zones, the gas consumption of individual control zones, the oxygen content, the pressure in the furnace, the holding time of a billet at a particular position in the furnace (**Figure 6**), can be selected. The archive mode allows a preview of the reheating process

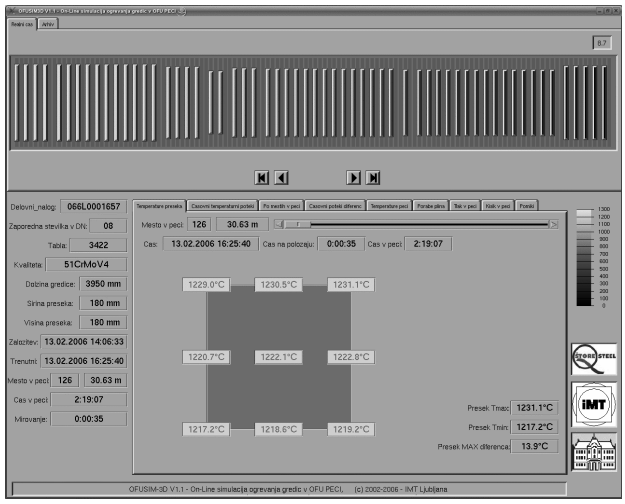

Figure 5: The human-machine interface of the simulation model – calculated temperatures of characteristic points of the cross-section
Slika 5: Grafični uporabniški vmesnik simulacijskega modela – izračunane temperature karakterističnih točk prereza

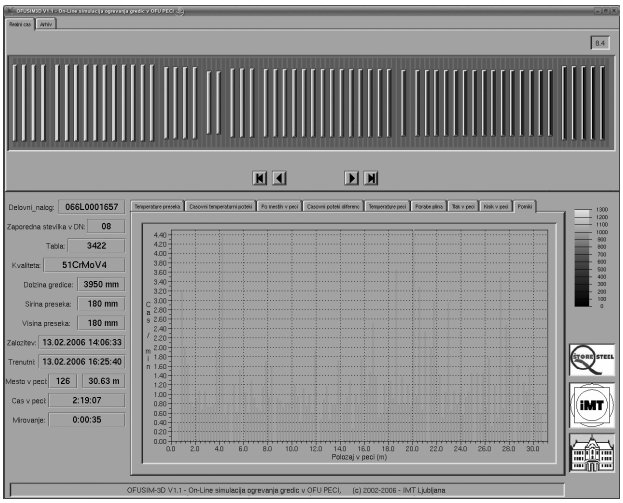

Figure 6: The human-machine interface of the simulation model – diagram of the residing time of the billet at a particular position in the furnace

Slika 6: Grafični uporabniški vmesnik simulacijskega modela – diagram časa zadrževanja gredice na posameznem mestu v peči

of already-reheated billets. Billets in the archive list are sorted by discharge time. The HMI is developed using the XFORMS graphical library.

3 RESULTS AND DISCUSSION

The model was validated on the basis of measurements from the OFU walking-beam furnace at the Štore Steel steelworks in Slovenia. The test billet (CK45 steel grade, dimensions 140 mm x 140 mm x 3500 mm) was reheated during the normal production process. The temperature measurements were performed using five trailing thermocouples (Type K, ϕ = 4.5 mm, L = 35 m). These five thermocouples were mounted inside a test billet, as shown in **Figure 7**. Thermocouple TC1 was mounted 10 mm under the upper slab surface; TC2 was mounted 10 mm from the left billet surface, 70 mm deep; TC2 was mounted 10 mm from the right billet surface, 70 mm deep; TC4 was mounted 10 mm from the bottom billet surface, 130 mm deep; and TC5 was mounted in the centre of the billet.

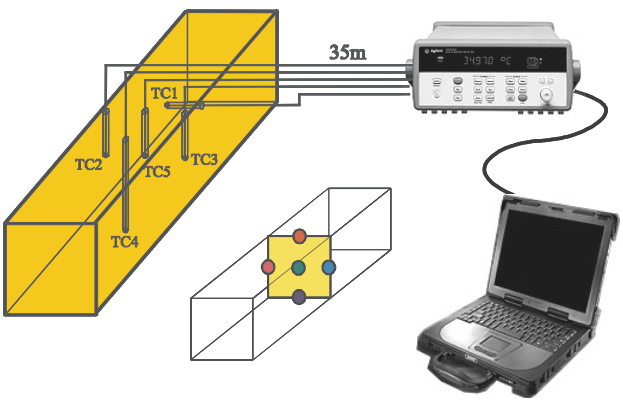

Figure 7: Measuring points in the test billet

Slika 7: Merilne točke na preizkusni gredici

The simulation model was compared with the measurements at all five measuring points, TC1, TC2, TC3, TC4 and TC5. The model was tuned by adjusting the temperature profile of the furnace's ceiling and sidewalls. After tuning the model, all the parameters of the model were observed to be real physical values. Good agreement was obtained between the measured and the calculated temperatures at all five comparison points for the whole reheating process (**Figures 8 and 9**). The graph was divided into two graphs–the first for the time interval 0–60 min (**Figure 8**) and the second for the time interval 60–120 min (**Figure 9**) – in order to distinguish between the measured and the calculated values. The small vertical lines at the bottom of the graphs show the walking-beam step intervals of the furnace.

The validation phase shows that the developed algorithms of the simulation model for billet reheating in

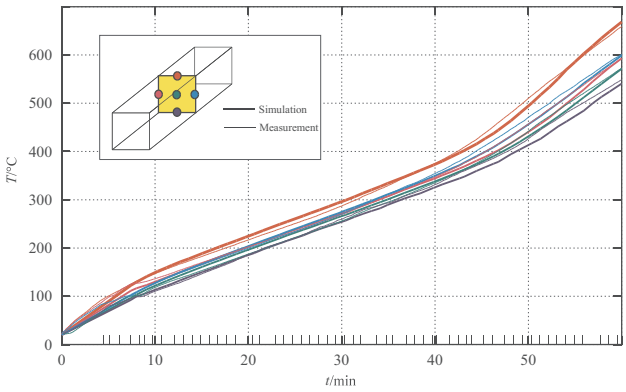

Figure 8: Validation of the simulation model for the test billet (material: CK45, 140 mm x 140 mm x 3500 mm) for the time interval 0–60 min

Slika 8: Vrednotenje simulacijskega modela na preskusni gredici (material: CK45, 140 mm x 140 mm x 3500 mm) v časovnem intervalu 0–60 min

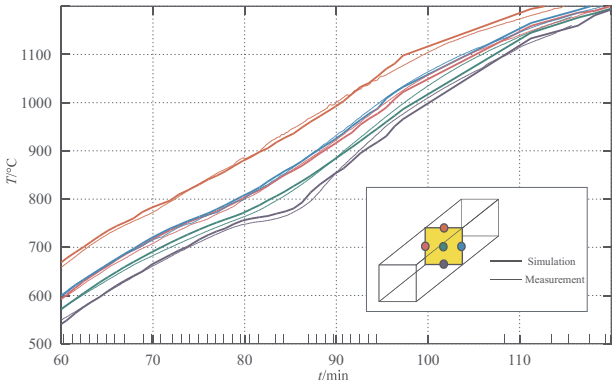

Figure 9: Validation of the simulation model for the test billet (material: CK45, 140 mm x 140 mm x 3500 mm) for the time interval 60–120 min

Slika 9: Vrednotenje simulacijskega modela na preskusni gredici (material: CK45, 140 mm x 140 mm x 3500 mm) v časovnem intervalu 60–120 min

the OFU furnace are in good agreement with the real physical behavior of the reheating process.

The system was developed using only open-source solutions, and the Linux platform ensures stable running of the system. The system has been used online in the regular production process at the Štore Steel, d. o. o. steelworks in Slovenia since May 2006.

4 CONCLUSIONS

The implemented system allows online monitoring of non-measurable values (the 3D temperature fields of billets in the furnace). The system is connected to the furnace-process computer to ensure real-time measuring and charging data from the furnace.

The simulation model's results are stored in an SQL database, which allows internet access to the data. Good agreement between the measured and the calculated heating curves shows that the model includes the main physical phenomena occurring during the reheating process in the OFU walking-Beam furnace. The developed HMI allows a user-friendly presentation of the simulation model's results. The system has been used online in the regular production process at the Štore Steel, d. o. o., steelworks in Slovenia since May 2006.

5 REFERENCES

[1] Staalman, D. F. J.: Process control in reheating furnaces, IoM Conference Challenges in Reheating Furnaces, Conference Papers, October 2002, London, 267–285

[2] Dahm, B., Klima, R.: Feedback control of stock temperature and oxygen content in reheating furnaces, IoM conference Challenges in Reheating Furnaces, Conference Papers, October 2002, London, 287–296

[3] Kolenko, T.; Glogovac, B., Jaklic, A.: An analysis of a heat transfer model for situations involving gas and surface radiative heat transfer. Commun. numer. methods eng., 15 (**1999**), 349–365

[4] Jaklič A., Kolenko T., Glogovac B.: Supervision of slab reheating process using mathematical model, 3rd IMACS Symposium on Mathematical Modelling MATHMOD, February 2–4, Vienna. Proceedings, (ARGESIM Report No. 15), Vienna, 2 (**2000**), 755–759

[5] Leden, B., Lindholm, D. and Nitteberg, E.: The use of STEEL-TEMP® software in heating control, La Revue de Métallurgie-CIT, 96 (**1999**) 3, 367–380

[6] Leden, B.: STEELTEMP® for temperature and heat-transfer analysis of heating furnaces with on-line applications, IoM Conference Challenges in Reheating Furnaces, Conference Papers, October 2002, London, 297–307

[7] ECSC Steel RTD Programme, Contract No. 7210-PA/278, 7210-PB/278, 7210-PC/278, Rules based system for the improved monitoring and guidance of reheating furnaces

[8] Jaklič A., Kolenko, T., Glogovac, B.: A real-time simulation model of billet reheating in the Allino walking-beam furance. Zborník referátov : žiaromateriály, pece a tepelné izolácie: refractories, furnaces and thermal insulations. Košice: Hutnícka fakulta Technickej univerzity, 2004, 237–242

[9] Jaklič A., Vode F., Robič R., Perko F., Strmole B., Novak J., Triplat J.: The implementation of an online mathematical model of slab reheating in a pusher-type furnace *Mater. tehnol.*, 39 (**2005**) 6, 215–220

[10] Jaklič A., Kolenko T., Zupančič B.: The influence of the space between the billets on the productivity of a continuous walking-beam furnace. *Appl. therm. eng.*. [Print ed.], 25 (**2005**) 5–6, 783–795

[11] Heiligenstaedt W.: Wärmetechnische Rechnungen für Industrieöfen, Verlag Stahleisen mbH, Düsseldorf, 1966

UDC/UDK 621.791.05:620.178.152.3
Original scientific article/Izvirni znanstveni članek

ISSN 1580-2949
MTAEC9, 41(3)125(2007)

THE BEHAVIOUR OF COARSE-GRAIN HAZ STEEL WITH SMALL DEFECTS DURING CYCLIC LOADING

VEDENJE JEKLA GROBOZRNATEGA TVP Z NAPAKAMI PRI CIKLIČNI OBREMENITVI

Vladimir Gliha, Tomaž Vuherer

University of Maribor, Faculty of Mechanical Engineering, Smetanova 17, 2000 Maribor, Slovenia
vladimir.gliha@uni-mb.si/ tomaz.vuherer@uni-mb.si

Prejem rokopisa – received: 2006-05-17; sprejem za objavo – accepted for publication: 2007-01-15

The effects of small, artificial surface defects on the fatigue strength of coarse-grain HAZ material found at the weld toe were studied. The size of the defects did not exceed the grain size, which is the most relevant microstructural unit of polycrystalline metals. The artificial defects were made by indenting the material with a Vickers pyramid and by drilling holes. The samples of coarse-grain HAZ material were prepared using a welding thermal-cycle simulator or a furnace.
The experimentally determined bending fatigue strength versus the properly evaluated defects size was compared with the propagation of long cracks. Residual stresses appear when making small artificial defects. The crack initiation from the defects was analysed and the influence of residual stresses is discussed.

Key words: HAZ, weld toe, coarse grain, fatigue strength, artificial defect, residual stresses, non-propagating crack

Raziskan je bil vpliv majhnih umetnih napak na dinamično trdnost grobozrnatega dela TVP ob robu zvarov. Napake niso bile večje od kristalnih zrn, ki so najbolj pomembna enota polikristalnih materialov. Umetne napake smo ustvarili z odtiskovanjem Vickesove piramide in vrtanjem. Preizkušance z grobozrnatim jeklom TVP smo pripravili v simulatorju termičnega cikla in v peči.
Eksperimentalno določeno upogibno dinamično trdnost v odvisnosti od velikosti napake smo primerjali s propagacijo dolgih razpok. S pripravo umetnih napak nastanejo zaostale napetosti. V razpravi je govor o začetku razpoke iz napak in o vplivu zaostalih napetosti.

Ključne besede: TVP, rob zvara, groba zrna, dinamična trdnost, umetne napake, stabilna razpoka

1 INTRODUCTION

Defects decrease the fatigue strength of welds. In the past, S-N curves were the only available tool to predict the fatigue life of real quality welds until LEFM concepts started to be applied to welds with macroscopic crack-like defects.

Murakami and co-workers treated the influence of variously shaped small defects in the same way as cracks, i.e., using LEFM concepts [1–3]. The square root of the projection of defects onto the plane perpendicular to the cyclic stress is a parameter reflecting the effect of small defects on the fatigue strength of metallic materials. However, LEFM greatly underestimates the propagation rates of short cracks within the local plastic zones that develop as a result of the stress concentration [4,5].

Small cracks, much smaller than the smallest microstructural units (microstructurally small defects), have no influence on the fatigue strength of metals (endurance limit) although these cracks can propagate unexpectedly quickly at the beginning. Nevertheless, the propagation decelerates gradually when approaching microstructural obstacles such as grain boundaries. The propagation can even stop, and the cracks then become non-propagating. However, in the presence of cracks whose size is comparable to the microstructural units of a metal, the fatigue strength of metals is lowered. The behaviour of metals with cracks from the smallest (short cracks) to the biggest (long cracks) is described with the use of a Kitagawa-Takahashy diagram [6].

The crack-initiation times in the highest-quality butt-welds are shorter than predicted by LEFM if the cracks initiate at the weld toe. Therefore, the possibility of crack initiation at the weld toe, where a substantial stress concentration exists, is of greatest importance for the load-carrying capacity of cyclically loaded welded structures (**Figure 1**). Because of the concentrated stress,

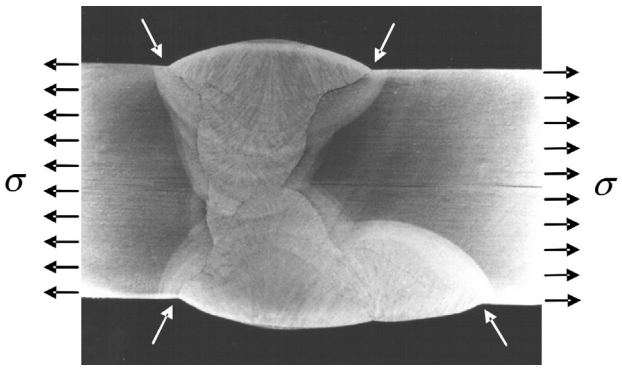

Figure 1: Macrograph of a K-butt weld with a remote homogeneous stress. Arrows indicate the weld toes: the positions of the concentrated stress field.

Slika 1: Makrografija K-zvara s homogeno napetostjo daleč od spoja. Puščice označujejo robove zvarov in položaj koncentriranega polja napetosti.

Table 1: Simulation parameters, mechanical properties, microstructures and test conditions
Tabela 1: Parametri simulacije, mehanske lastnosti, mikrostrukture in pogoji preizkušanja

Designation	Cooling time *t*/s	Yield strength /MPa	Tensile strength /MPa	Grain size *d*/μm	Microstructure	Condition
M1	5	981	1210	130	M	C_1,C_2,C_3,C_4,C_6
M2	9	935	1171	140	M+B	C_1, C_2, C_4, C_6
M3	5.5	992	1192	180	M	C_1, C_2, C_4, C_6
M4	9.5	939	1176	140	M+B	C_1, C_2, C_4, C_5, C_6
M5	9.5	921	1172	180	M+B	C_1, C_2, C_4, C_5, C_6

cracks at the weld toe initiate in the coarse-grain region of the HAZ, the formation of which is the result of the heat input needed for the fusion welding and, as a rule, it is much harder than the base metal [7].

Artificial defects, especially small holes, are used with great success in studies of the effects of small defects on the endurance limit of metallic materials. Extremely small weld defects, such as sharp transitions, inclusions, scratches or cracks, present at the weld toe, i.e., in the coarse-grain HAZ, can be modelled with artificial defects, too.

Vickers indentations are suitable artificial defects. The preparation of a proper indentation of the prescribed size is easy to execute because only the hardness has to be known. The problem of Vickers indentations used as artificial weld defects is residual stresses. Any kind of defect made in a mechanical way results in the appearance of residual stresses. The reason is in the irreversibility of the plastic deformation, which is very extensive when indenting with Vickers pyramids. High residual stresses affect the local stress/strain conditions and change the actual shape of the artificial defect.

The behaviour of coarse-grain HAZ materials with different types of microstructurally small defects in a stress-concentrated condition was studied for cyclic loading. The effects of the residual stresses were taken into account.

2 EXPERIMENTAL

For this study samples of coarse-grained steel characteristic of the HAZ at the weld toe in the as-welded condition in the case of "cold" welding were prepared by simulating the thermal conditions in the material close to the weld on a welding thermal-cycle simulator (Smitweld). The coarse-grain microstructure was either pure martensite (M) or martensite with a small portion of bainite (M+B).

The simulated coarse-grain HAZ microstructures were designated as M1–M5. They were formed at different cooling rates. The data on the cooling times, the mechanical properties and the microstructures are shown in **Table 1**.

The specimens for the fatigue-strength testing were machined from samples with the simulated HAZ microstructure with the shape and size shown in **Figure 2**.

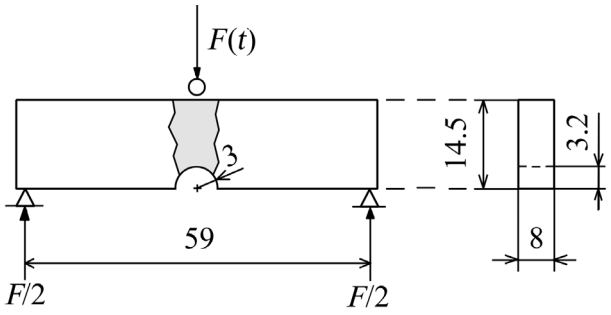

Figure 2: Bend specimen with a notch in the simulated coarse-grain HAZ steel
Slika 2: Upogibni preizkušanci z zarezo na področju z jeklom simuliranega grobozrnatega TVP

The specimens were notched in the region with the simulated HAZ microstructure. The bottom of the notch was ground and polished. The calculated stress concentration caused by the notch was 1.74. The smooth surface at the bottom of the notch is specified in Table 1 as test condition C_1.

Artificial defects of different sizes and shapes were made by indenting with a Vickers pyramid on the bottom of the notch. As shown in Figure 3, they were single indentations and a series of five indentations in a straight line, perpendicular to the testing stress.

The average size of the single indentations, *d*, was (105, 160, and 221) μm. These situations are specified in Table 1 as the test conditions C_2, C_3 and C_4.

The average length of a series of indentations, *l*, was 386 μm and 692 μm. These situations are specified in Table 1 as the test conditions C_5 and C_6. The series were composed of indentations with diagonals of length of approximately 110 μm and 220 μm.

In the second part of this study, a coarse-grain HAZ was prepared with furnace heating. During the first step the samples of steel were heated to 1100 °C and held for 3 h. The grains grew to a size of 200 μm. This coarse-grain annealing was followed by cooling in water. The next step of the thermal treatment was heating to 870 °C and water quenching. The result of the combined thermal treatment was a microstructure of pure martensite.

The specimens were notched and artificial defects made either before or after the quenching.

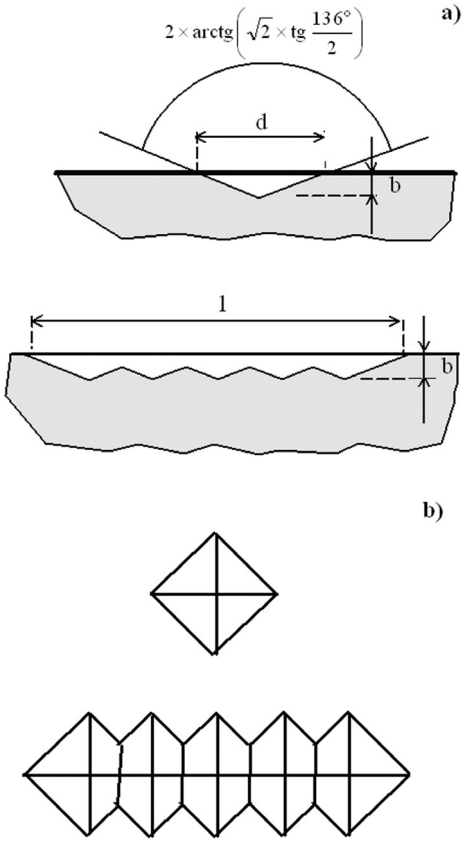

Figure 3: Small artificial surface defects: a single indentation with diagonal *d* and a series of five indentations with length *l* (cross-section – a, ground plan – b)

Slika 3: Majhne umetne površinske napake: odtis z diagonalo d in niz petih odtisov z dolžino l (prerez – a, naris – b)

3 EXPERIMENTAL RESULTS AND DISCUSSION

Smooth and artificially surface-defected specimens were bend-loaded in the first part of this study on a resonant machine at room temperature in the load-control mode. The frequency of the loading and the stress rate were $f \cong 115$ Hz and $R \cong 0$, respectively.

The loading was increased in steps to 2 million cycles or to fatigue crack initiation or specimen fracture. A new specimen was used each time. The results of the testing were S-N curves, valid for the test condition C_1–C_6, and the coarse-grain HAZ materials M1–M5. The highest stress range, $\Delta\sigma_B$, at which the material still resisted after 2 million cycles was taken as the bending fatigue strength of the material, $\Delta\sigma_{f\text{-}B}$. The numerical results of the testing are shown in **Table 2**.

The depth of the artificial defects, *b* in **Figure 3**, is an important parameter for the $\sqrt{\text{area}}$ evaluation, which depends on the size of the indentation. The angle between the opposite planes at the top of the Vickers pyramid is 136°. The angle, α, between the opposite edges that form the diagonal of the indentation, is therefore somewhat bigger:

$$\alpha = 2\text{arctg}\,(\sqrt{2}\cdot\text{tg}\frac{136°}{2});\; b = \frac{d\sqrt{2}}{4}\cdot\text{ctg}\frac{136°}{2} \qquad (1)$$

The defect size parameter $\sqrt{\text{area}}$ was evaluated for each of the used artificial defects, single indentations of three sizes and a series of indentations of two sizes. A special approach for the evaluation of long-shallow small defects is available [8].

As shown in **Figure 4**, the area is the plane of the actual defect projection for the single indentation and the product of the maximum defect width with the length of ten times the depth for the series of indentations [8].

$$area|_{\text{ind}} = \frac{d^2\sqrt{2}}{8}\text{ctg}\frac{136°}{2};\; area|_{\text{ind}} = \frac{5d^2\sqrt{2}}{4}\text{ctg}^2\frac{136°}{2} \qquad (2)$$

The relationships between the results of the testing expressed as the fatigue strength $\Delta\sigma_{f\text{-}B}$ and the parameter $\sqrt{\text{area}}$ are shown on a logarithmic-logarithmic scale in **Figure 5**.

The shapes of the curves in **Figure 5** agree quite well with the Kitagawa-Takahashy plot. For that reason, three dotted lines are entered in the figure, representing the possible fatigue strengths of coarse-grained HAZ materials with long cracks. One of these lines could be the right-hand side of the Kitagawa-Takahashy plot because

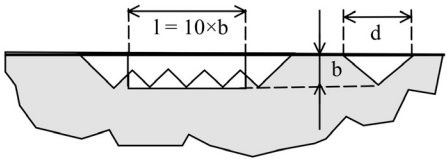

Figure 4: Size of the image of a series of indentations and a single indentation

Slika 4: Velikost ploščine niza odtisov in enega odtisa

Table 2: Fatigue strength of the HAZs in terms of the quality of the surface at the bottom of the notch

Tabela 2: Trajna dinamična trdnost TVP pri različni kakovosti površine na dnu zareze

Test condition	C_1	C_2	C_3	C_4	C_5	C_6
Defect size, μm	0	$d \cong 105$	$d \cong 160$	$d \cong 221$	$l \cong 386$	$l \cong 692$
Material	$\Delta\sigma_{f\text{-}B}$/MPa					
M1	539	526	520	481	–	442
M2	546	507	–	468	–	442
M3	533	520	–	468	–	416
M4	533	533	507	442	–	416
M5	526	520	–	468	481	416

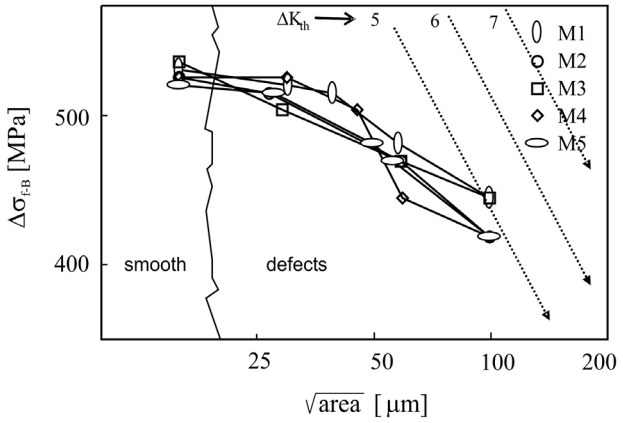

Figure 5: Dependence of the bending fatigue strength on the defect size parameter $\sqrt{\text{area}}$, calculated as illustrated in **Figure 4**

Slika 5: Odvisnost med upogibno dinamično trdnostjo in parametrom velikosti napake $\sqrt{\text{area}}$, izračunananim tako, kot je prikazano na **sliki 4**

the ΔK_{th}-value for carbon structural steels corresponds to 5–10 MPa $\sqrt{\text{m}}$.

Smooth and artificially surface-defected specimens were bend-loaded in the second part of this study on a rotary bending machine at room temperature in the load-control mode. The frequency of the loading and the stress rate were $f \cong 100$ Hz and $R = -1$, respectively. Single Vickers indentations and drilled small holes were used as artificial weld defects. The defect size parameter $\sqrt{\text{area}}$ was the same for both types of defect. Two examples of these defects with already-initiated cracks are shown in **Figures 6 and 7**.

The life of fatigue cracks has two stages: initiation and propagation. The crack initiation from defects in the presence of residual stresses is either easier or more difficult because of the locally enhanced or reduced stress/strain field caused by the defect preparation. Due to the existing pre-stress, the local stress rate, R, is changed. During the fatigue loading, at a sufficiently high stress level, cracks appear due to the interactive effect of the micro-defect and the loading.

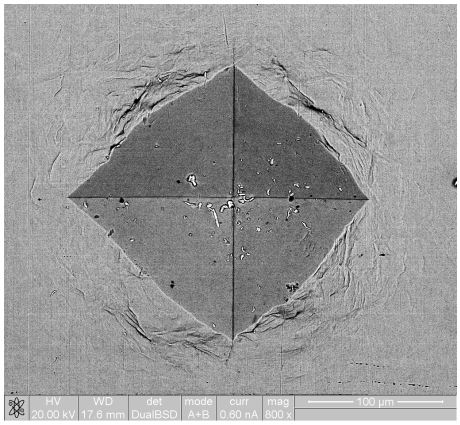

Figure 6: Vickers indentation with a diagonal of 200 μm. Cracks are visible at the ends of the indentation.

Slika 6: Vickers odtis z diagonalo 200 μm. Razpoki vidimo na konceh odtisa.

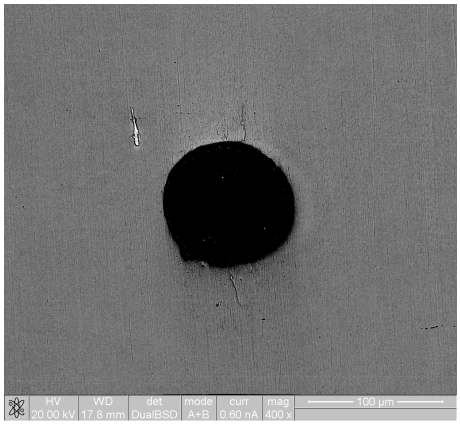

Figure 7: Drilled hole with a diameter of 90 μm. Cracks are initiated on both sides of the hole.

Slika 7: Izvrtina s premerom 90 μm. Razpoki nastaneta na obeh straneh izvrtine.

To distinguish between the effects of microstructurally small defects assisted by local residual stresses and microstructurally small defects acting alone, a suitable approach to remove those stresses was necessary. Electro-etching was not effective enough with indentations, although it is often used with drilled holes. Recrystallization in the last stage of CGHAZ simulation using a furnace seemed a convenient way to remove the local residual stresses without significantly changing the defect's geometry.

Two kinds of specimens with artificial defects were prepared:

- specimens in the as-indented or as-drilled condition
- specimens in the stress-relieved condition

Local residual stresses due to indenting are compressive, whilst with drilling they could be tensile. When the defect is made before heating for water quenching, local residual stresses do not exist after quenching. The reason is the newly formed microstructure, caused by recrystallization during the transformation. In contrast, the introduction of the defect after the complete thermal treatment for coarse-grain HAZ simulation induces local residual stresses.

In the first stage of fatigue testing, a microcrack appears either at the surface, adjacent to the defects, or inside the defects. Crack initiation occurs in individual grains where the cyclic tangential stress in the weakest crystal plane of randomly oriented grains exceeds a determined level. If the remote stress level is not too high the grain boundary arrests the crack propagation. Local stress concentration due to the presence of defects assists the crack initiation, but the effect is reduced with the distance.

An array of initiated cracks on a specimen with a smooth surface is seen in **Figure 8**. The cracks are not longer than the average grain size, i.e., 200 μm. Their orientation in the initiation stage is close to $\pm \pi/4$.

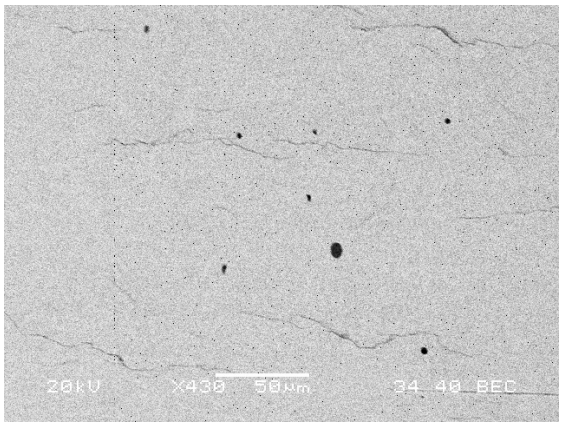

Figure 8: Cracks initiated at the bottom of the notched specimen without defects
Slika 8: Razpoke, ki so nastale na dnu zareze, ko ni napak

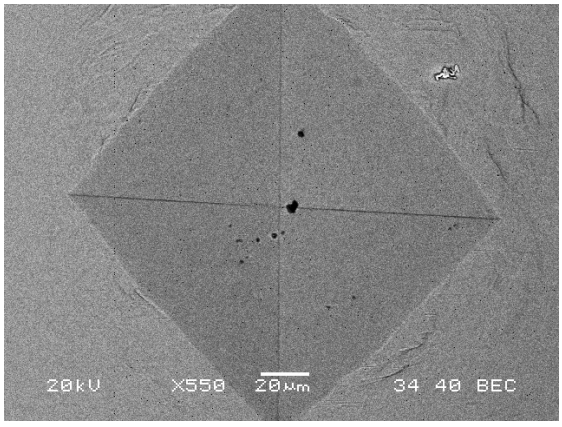

Figure 9: Two cracks initiated at both edges of a Vickers indentation
Slika 9: Razpoki, ki sta nastali na obeh robovih Vickers odtisa

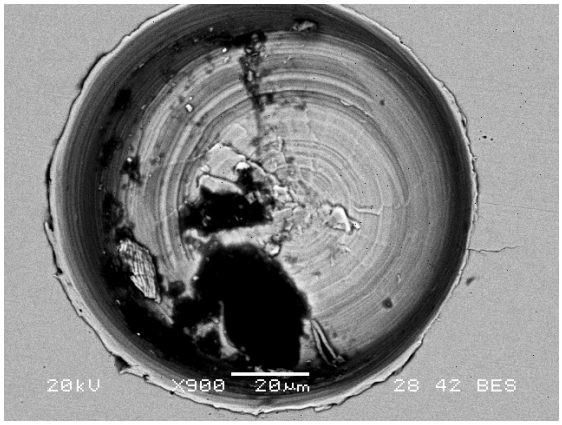

Figure 10: A single crack initiated from a hole
Slika 10: Ena sama razpoka, ki je nastala na izvrtini

In specimens where the crack is defected initiation turns up in part of the grains where the intensity of the cyclic stress/strain field is sufficient and it is parallel to the shearing direction of the grain.

Figure 9 represents two separate cracks initiated at the edges of the indentation. They are not connected at the bottom of the indentation and did not spread over the surface outside the indentation like the crack shown in **Figure 6**. The reason for this is the existence of compressive residual stresses, mostly at the bottom of the indentation.

Figure 10 shows a single crack initiated at the edge of a round hole. The difference between the two cracks in **Figure 7** and the single crack in **Figure 10** is explained by the absence of tensile residual stresses in the close vicinity of the hole. Only the grain with the initiated crack was oriented to enable crack initiation, the orientation of the grain on the other side was less suitable.

4 CONCLUSIONS

The shape of the relationship curve presenting the bending fatigue strength, $\Delta\sigma_{f\text{-}B}$, versus the defect size parameter $\sqrt{area}$ shown in Figure 5 does not approach the expected linear trend defined with several ΔK_{th}-values up to the defect size parameter $\sqrt{area} \cong 100\ \mu m$. This is not surprising, because the threshold stress-intensity factor, ΔK_{th}, which defines the fatigue strength of materials with macroscopic cracks (the long-crack propagation law) is grain-size dependent. Because of coarse grains the ΔK_{th}-value is very likely much higher than 7. On the other hand, it seems that the defect size parameter $\sqrt{area}$ underestimates the fatigue strength, thereby lowering the effect of a series of indentations.

At this point it is not possible to conclude what is more important for the unexpected shape of the relationship curve $\Delta\sigma_{f\text{-}B}$-$\sqrt{area}$, the coarse grain size or the indenting residual stresses. The length of the biggest series of indentations is almost 700 µm (4–6 times the average grain size); the depth of the indentations does not exceed 31–32 µm (much less than the average grain size). A logical question is which extension of the series of indentations, length or depth, is more important? The answer – that it depends on which direction the cracks initiate – seems to be doubtful.

It was expected that specimens in the as-indented condition would behave differently than those in the stress-relieved condition. The reason is the presence of the residual stresses:

If compressive residual stresses are the highest at the deepest part of the indentation, cracks will initiate separately at both loaded edges of the indentation. When the stress level is sufficiently low those cracks become non-propagating after their initiation. When stress level is higher the cracks join at the deepest part of the indentation and create a single crack. The effect of a bigger single crack is greater than the effect of separate cracks, although its size is almost equal to the sum of their lengths.

In the absence of residual stresses the crack will initiate as a single crack over the whole length of the indentation. An initiated crack in the stress-relieved condition that is longer than the indentation diagonal has a stronger effect than the effect of two separate cracks in the as-indented condition. The higher fatigue strength of the specimens with compressive residual stresses than those without residual stresses is logical.

Hole-drilled specimens behave differently than indented specimens. The residual stresses due to drilling are tensile; therefore, the opposite behaviour by the drilled specimens was observed. The fatigue strength of specimens with residual stresses is lower than the fatigue strength of specimens without residual stresses.

Generally, compressive stresses at the surface increase the fatigue strength, while the tensile stresses decrease it.

5 REFERENCES

[1] Murakami, Y. at al. Quantitative evaluation of effects of non-metallic inclusions on fatigue strength of high strength steels – I: Basic fatigue mechanism and evaluation of correlation between the fatigue fracture stress and the size and location of non-metallic inclusions, Int. J. of Fatigue, 9 (**1989**), 291–298

[2] Murakami, Y., Usuki, H. Quantitative evaluation of effects of non-metallic inclusions on fatigue strength of high strength steels – II: Fatigue limit evaluation based on statistics for extreme values of inclusion size, Int. J. of Fatigue, 9 (**1989**), 299–308

[3] Murakami, Y. Effects of small defects and nonmetallic inclusions on fatigue strength of metals, JSME International Journal I, 32 (**1989**) 2, 167–180

[4] Miller, K. J. The behaviour of short fatigue cracks and their initiation, Part I and Part II, Fatigue Fract. Engng. Mater. Struct., 10 (**1987**) 1, 75–91 and 10 (**1987**) 2, 93–113

[5] Yasniy P-V. at al. Microcrack initiation and growth in heat-resistant 15Kh2MFA steel under cyclic deformation, Fatigue Fract. Engng. Mater. Struct., 28 (**2005**) 4, 391–397

[6] Kitagawa, H., Takahashi, S. Applicability of fracture mechanics to very small cracks or the cracks in the early stage, 2nd International Conference on the Behaviour of Materials, Boston, ZDA, 1976

[7] Verreman, Y., Bailon, J-P., Masounave, J. Fatigue life prediction of welded joints – A re-assessment, Fatigue Fract. Engng. Mater. Struct., 10 (**1987**) 1, 17–36

[8] Murakami, Y., Endo, M. Effects of hardness and crack geometries on ΔK_{th} of small cracks emanating from small defects, The behaviour of short fatigue cracks, Edited by K. J. Miller, E. R. de los Rios, Mechanical Engineering Publications, 1986

UDC/UDK 669.14.018.8:620.193
Original scientific article/Izvirni znanstveni članek

ISSN 1580-2949
MTAEC9, 41(3)131(2007)

THE EFFECT OF COLD WORK ON THE SENSITISATION OF AUSTENITIC STAINLESS STEELS

VPLIV HLADNE DEFORMACIJE NA POVEČANJE OBČUTLJIVOSTI NERJAVNIH JEKEL

Mária Dománková, Marek Peter, Moravčík Roman

Faculty of Materials Science and Technology in Trnava, Slovak University of Technology in Bratislava,
Bottova 24, 917 24 Trnava, Slovakia
maria.domankova@stuba.sk

Prejem rokopisa – received: 2006-09-20; sprejem za objavo – accepted for publication: 2007-01-15

The sensitisation behaviour of austenitic stainless steel is greatly influenced by several metallurgical factors, such as the chemical composition, the degree of prior deformation, the grain size, and the ageing temperature and time. The precipitation behaviour of AISI 316 and 304 austenitic stainless steels has been investigated after ageing at various temperatures from 500 °C to 900 °C for 0.1 h to 1000 h. The TTS diagrams of the experimental steels after an oxalic-acid etch test ASTM A262 practice A were constructed. It was demonstrated that the C curves of the TTS diagrams were displaced towards shorter times by the increment of 20 % cold work (CW), since the sites inside the grain matrix have a high energy and the carbides can nucleate there easily. Cold work increases the number of dislocations/dislocation pipes along which the diffusion rate of chromium is very high. The sensitisation of the experimental steels accelerated the precipitation of $M_{23}C_6$. Besides $M_{23}C_6$, the σ-phase and M_6C were detected at the grain boundaries and in the austenitic matrix in the case of the cold-worked samples.

Key words: austenitic stainless steels, sensitisation, precipitation, cold working, intergranular corrosion

Občutljivost nerjavnih jekel je odvisna od več metalurških dejavnikov, npr. od kemične sestave, predhodne deformacije, velikosti zrn, časa in temperature staranja. Izločilno vedenje jekel AISI 316 in 304 je bilo raziskano po različno dolgem staranju od 0,1 h do 1000 h pri temperaturah med 500 °C in 900 °C. TTS diagrami eksperimentalnih jekel so bili pripravljeni po oksalnem preizkusu po ASTM 262 – metoda A. Dokazano je, da so C-krivulje TTS-diagramov premaknjene h krajšim časom po 20-odstotni hladni deformaciji (CW), zato ker imajo tudi v zrnih mesta z veliko energijo, kjer nastanejo karbidni izločki. Hladna deformacija poveča število dislokacij/dislokacijskih cevk, kjer je difuzija kroma zelo hitra. Povečanje občutljivosti jekel je povečalo hitrost izločanja karbidov $M_{23}C_6$. σ-fazo in M_6 karbide smo v hladno deformiranem jeklu opazili ob kristalnih mejah in v avstenitni matrici.

Ključne besede: avstenitna nerjavna jekla, povečanje občutljivosti, hladna deformacija, interkristalna korozija

1 INTRODUCTION

The intergranular corrosion (IGC) and stress-corrosion cracking (SCC) of austenitic stainless steels are the most important corrosion processes that affect the service behaviour of these materials. Exposure to temperatures in range 500–800 °C leads to the grain-boundary precipitation of chromium-rich carbides $(Fe,Cr)_{23}C_6$ and to the formation of chromium-depleted regions. If the mass fraction of chromium content near the grain boundaries drops under the passivity limit of 12 %, the steel becomes sensitised. The sensitisation temperature range is often encountered during isothermal heat treatment, slow cooling from the solution annealing temperature, the improper heat treatment in the heat-affected zone of the welds or welding joints or the hot working of the material. The degree of sensitisation (DOS) is influenced by factors such as the steel's chemical composition, the grain size, the degree of strain or temperature and the time of isothermal annealing. The sensitisation involves both the nucleation and growth of carbides at the grain boundaries. Depending on the state or the energy of the grain boundaries they can provide preferential sites for carbide nucleation and act as a favoured diffusion path for the growth of carbides. Therefore, it has been suggested that the nature of grain boundaries could also influence the DOS and IGC [1–4].

In this article we report on some preliminary comparisons of the combined effects of chemical composition, deformation, temperature and aging time on sensitisation in AISI 304 and 316 stainless steels.

2 MATERIALS AND EXPERIMENTAL PROCEDURES

The chemical composition of the experimental steels is given in **Table 1**. The steels were mostly investigated in the as-received condition with some in the solution-annealed condition. The solution annealing was conducted on the as-received materials at 1050 °C for 60 min followed by water quenching.

The steels were 20–40 % cold rolled by controlling the thickness of the plates. The cold-worked samples were heat treated at various temperatures in the range 500–900 °C for times of 0.1 to 1000 h. The samples were then water quenched after the heat treatment.

The oxalic-acid etch test (ASTM A262 practice A) was used to determine the steels' sensitivity to inter-granular corrosion. The specimens were electrolytically etched in 10 % oxalic acid for 90 s at a current density of

Table 1: Chemical composition (in mass fractions, *w*/%) of the austenitic stainless steels
Tabela 1: Kemična sestava (v masnih deležih, *w*/%) avstenitnih nerjavnih jekel

steel	C	N	Si	Mn	P	S	Cr	Ni	Mo	Fe
AISI 304	0.04	0.012	0.54	1.08	0.0032	0.008	18.52	8.47	0.21	bal.
AISI 316	0.05	0.032	0.47	0.86	0.0026	0.001	17.55	11.56	2.10	bal.

1 A/cm^2. The etched microstructure was then examined at 250x, and was characterised as a step, dual or ditch microstructure [5].

For the individual secondary-phase identification transmission electron microscopy (TEM) of the carbon extraction replicas was applied. TEM observations were performed using a JEOL 200 CX operating at 200 kV. The carbon extraction replicas were obtained from mechanically polished and etched surfaces. The replicas were stripped from the specimens in the solution of $CH_3COOH : HClO_4 = 4 : 1$ at 20 °C and 20 V.

3 RESULTS

The results of the light microscopy examination are summarised in **Figure 1**. The microstructure of AISI 304 after solution annealing consists of polyhedral austenitic grains with twinning typical of an fcc microstructure. The average austenitic grain size in this state is about 45 μm (**Figure 1a**). A small amount of δ-ferrite was also observed. No precipitates were detected at the grain boundaries (GBs) of the solution-annealed steels. **Figure 1b** shows the microstructure of the AISI 304 after 40 % of CW. The microstructures of the aged states are shown in **Figure 1c** and **Figure 1d**. **Figure 1c** shows the evolution of secondary phases precipitated at the

GB in the isothermally aged specimen (650 °C/0.5 h) without cold work. The microstructure of the isothermally aged specimen (650 °C/0.5 h) and 40 % CW is shown in Figure 1d. The precipitation of secondary phases was observed at the GB and intragranularly and within the matrix.

To compare the results of two austenitic stainless steels, time-temperature-sensitisation (TTS) diagrams for these steels for different degrees of CW ranging from 0 % to 40 % are presented in **Figure 2**. From the TTS diagrams it can be seen that the nose of the C curve corresponding to the maximum rate of sensitisation

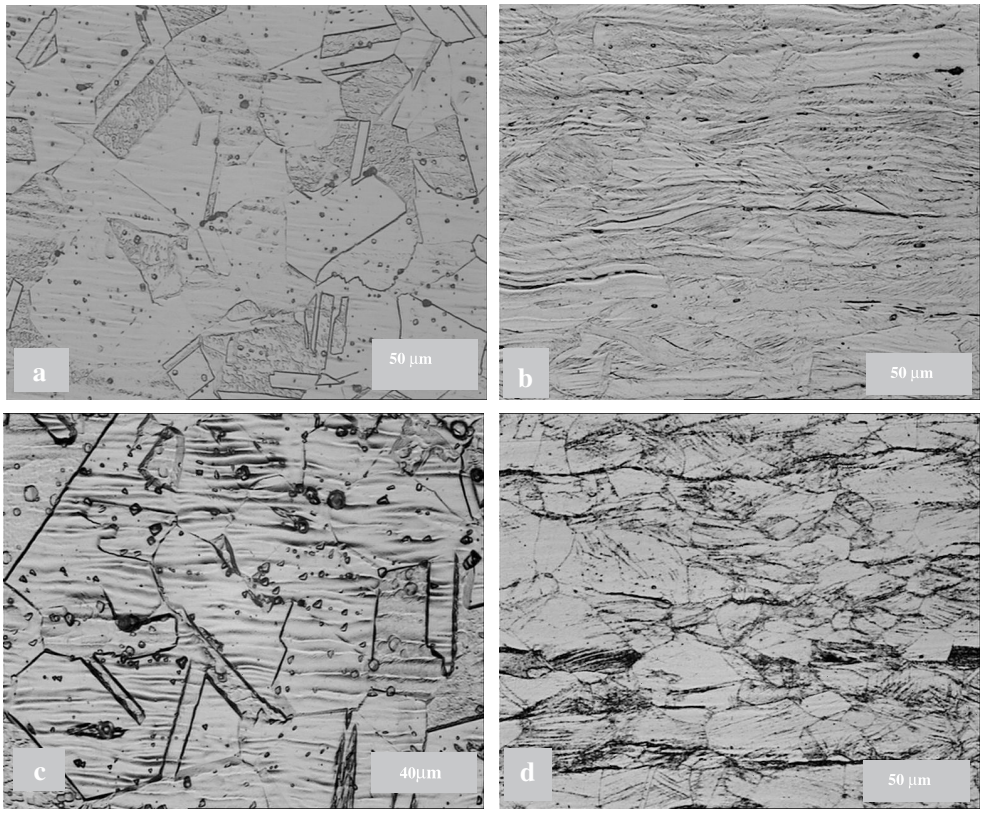

Figure 1: Microstructure of the AISI 304 a) after solution annealing – 0 % CW, b) after solution annealing – 40 % CW, c) after aging at 650 °C/0.5 h, 0 % CW, d) after aging at 650 °C/0.5 h, 40 % CW
Slika 1: Mikrostruktura jekla AISI 304 a) po topilnem žarjenju – 0 % CW, b) po topilnem žarjenju – 40 % CW, c) po staranju 650 °C/0,5 h, 0 % CW, d) po staranju 650 °C/0,5 h, 40 % CW

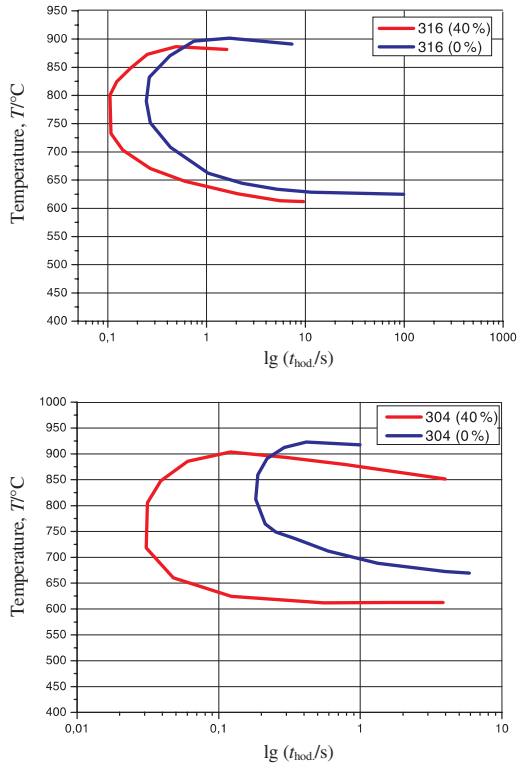

Figure 2: TTS diagrams for AISI type 316 and 304 stainless steels with various degrees of CW established as per ASTM A262 practice A test

Slika 2: TTS diagrama za nerjavni jekli 316 in 304 pri različni stopnji deformacije, določeni z ASTM A262-preizkusom

occurs at 800 °C for the AISI 316 in the 0 % CW condition. As the degree of CW increases, the nose temperature remains almost that same, but t_{min} decreases with the increase in % CW up to 20 % and remains constant thereafter. The TTS diagram of AISI 304 is shifted towards shorter times than the 0 % CW material. The tendency of the shift of the AISI 304 C curve is similar to the case of AISI 316.

To identify the type of secondary phases precipitated at the grain boundaries (GBs) during the isothermal

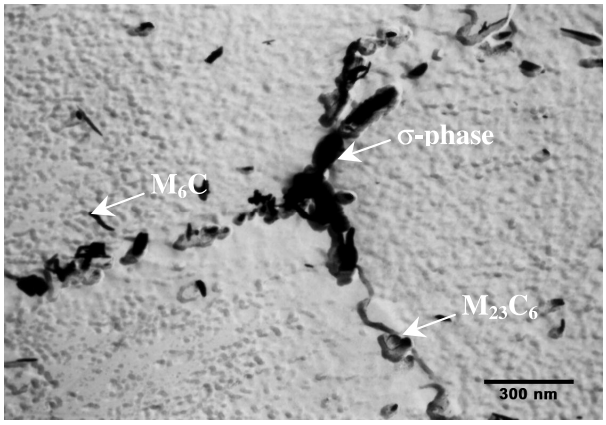

Figure 3: Microstructure of AISI 316 (650 °C/300 h) – TEM

Slika 3: Mikrostruktura jekla AISI 316 (650 °C/300 h) – TEM

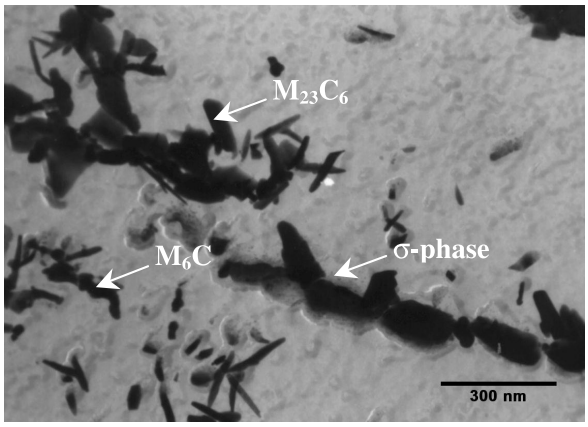

Figure 4: Microstructure of AISI 316 (650 °C/1000 h) - TEM

Slika 4: Mikrostruktura jekla AISI 316 (650 °C/1000 h) – TEM

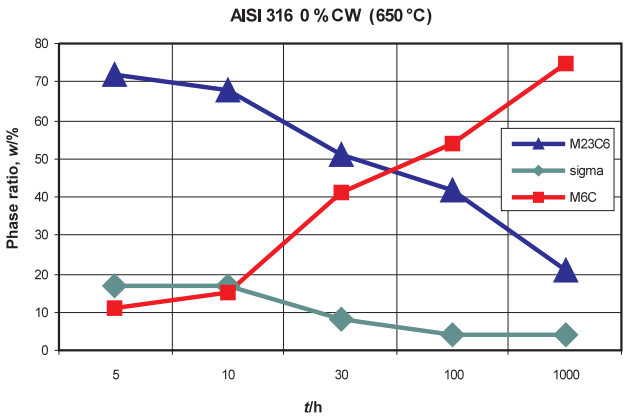

Figure 5: Phase ratio in AISI 316 after aging at 650 °C

Slika 5: Razmerje faz v jeklu AISI 316 po staranju pri temperaturi 650 °C

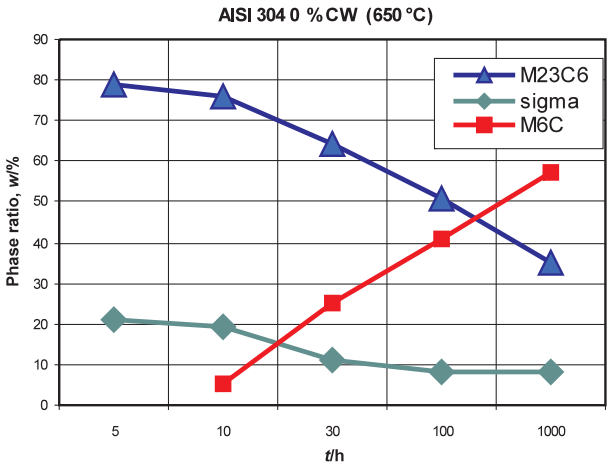

Figure 6: Phase ratio in AISI 304 after aging at 650 °C

Slika 6: Razmerje faz v jeklu AISI 304 po staranju pri temperaturi 650 °C

treatment, TEM analysis was carried out. First, $M_{23}C_6$ was detected at the grain boundaries after aging. In addition to $M_{23}C_6$, the σ-phase and M_6C were detected at the grain boundaries (**Figure 3 and Figure 4**). Similar precipitation trends were detected using TEM analysis at

the grain boundaries of the AISI 304 steel. The identified secondary phases in the experimental steels and the phase ratio are shown in **Figures 5 and 6**.

4 CONCLUSIONS

The precipitation behaviour of AISI 316 and 304 austenitic stainless steels was investigated during aging at various temperatures in range from 500 °C to 900 °C for times from 0.1 to 1000 h. The following conclusions can be drawn:

TTS diagrams of the experimental steels after the oxalic-acid etch test ASTM A262 practice A show that the C curves of the TTS diagrams are displaced towards shorter times with increasing amounts of CW.

After ≈20 % cold working, even the sites inside the grain matrix have high energy and carbides can nucleate there also. Cold work increases the number of dislocations/dislocation pipes along which the diffusion rate of chromium is faster.

Sensitisation of the experimental steels accelerated the precipitation of $M_{23}C_6$. In addition to this carbide, σ-phase and M_6C were detected at the grain boundaries and in the austenitic matrix in the cold-worked samples.

Acknowledgement

The authors wish to thank the Scientific Grant Agency of the Slovak Republic (VEGA) for their financial support of grant No. 1/2113/05.

5 REFERENCES

[1] Murr L. E. Advani A., Shakar S., Atteridge D. G.: Effects of deformation and heat treatment on grain boundary sensitisation and precipitation in austenitic stainless steels. *Material Characterization,* 24 (**1990**), 135–158

[2] Trillo E. A., Murr L. E.: Effects of carbon content, deformation and interfacial energetics on carbide precipitation and corrosion sensitisation in 304 stainless steel. *Acta Materialia,* 47 (**1999**) 1, 235–245

[3] Janovec J., Blach J, Záhumenský P., Magula V., Pecha J.: Role of intergranular precipitation in the fracture behaviour of AISI 316 austenitic stainless steel. *Canadian Metallurgical Quartely*, 38 (**1999**) 1, 53–59

[4] Parvathavartini N., Dayal R. K: Influence of chemical composition, prior deformation and prolonged thermal aging on sensitisation characteristics of austenitic stainless steels. *Journal of Nuclear Materials,* 305 (**2002**), 209–219

[5] Standard Practice for Detecting Susceptibility to Intergranular Corrosion of Austenitic Stainless Steels, ASTM, 2001

UDC/UDK 539.42
Original scientific article/Izvirni znanstveni članek

ISSN 1580-2949
MTAEC9, 41(3)135(2007)

FATIGUE-CRACK PROPAGATION NEAR A THRESHOLD REGION IN THE FRAMEWORK OF TWO-PARAMETER FRACTURE MECHANICS

DVOPARAMETRSKA LOMNO MEHANSKA ANALIZA HITROSTI UTRUJENOSTNE RAZPOKE BLIZU PRAGA PROPAGACIJE

Stanislav Seitl, Pavel Hutař

Institute of Physics of Materials, Academy of Sciences of the Czech Republic, Zizkova 22, 616 62 Brno, Czech Republic
seitl@ipm.cz

Prejem rokopisa – received: 2006-05-17; sprejem za objavo – accepted for publication: 2007-03-09

A two-parameter constraint-based fracture mechanics method was applied to the problems of the fatigue-crack propagation rate near a threshold region. Two geometries of specimens with different values of constraint were analyzed. The experimentally obtained results were compared with numerical data. The presented result makes it possible to relate experimentally measured data obtained from specimens with different geometries, and thus contributes to more reliable estimates of the residual fatigue life of a structure.

Key words: constraint, *T*-stress, threshold values, fatigue crack growth rate, high cyclic fatigue,

Dvoparametrska vpetostna metoda je uporabljena pri problemu širjenja utrujenostne razpoke blizu praga propagacije. Analizirani sta dve geometriji preizkušanca z različno vpetostjo. Eksperimentalni podatki so primerjani z numeričnimi. Rezultati omogočajo, da se poveča eksperimentalne izsledke s preizkušancev z različno geometrijo in omogočajo bolj zanesljivo oceno preostale trajnostne dobe neke strukture.

Ključne besede: vpetost, vrednosti praga, hitrost rasti utrujenostne razpoke, visokociklična utrujenost

1 INTRODUCTION

The understanding of constraint effects on the fatigue-crack propagation rate (FCPR) is relevant for the prediction of the operating life of engineering structures. The elastic *T*-stress, the second term of Williams's series expansion[1] for linear elastic crack-tip fields, represents the stress acting parallel to the crack plane. In paper[2] results relating to FCPR measurements for a 2024 aluminum alloy of two different specimen geometries are investigated. The FCPR was found to be sensitive to the specimen's geometry in the Paris region of the d*a*/d*N*–*K* curve as well as in the threshold values. The same trends are quantified for different levels of constraint in the vicinity of the fatigue-crack tip by means of the *T*-stress. This has been published for the ratio $R \approx 0$ in paper[3]. These findings are contradicted by the results published in [4]. The experiments are focused on the fatigue-crack growth data from three different specimen geometries obtained for nickel-based super-alloys and mild steel. The recently published study[5] describes experiments on edge-bending specimens SE(B) and C(T) specimens to characterize the fatigue-crack growth rates of Inconel 718, and in this study no difference in the crack-growth rate between the two kinds of specimens was observed.

Within two-parameter fracture mechanics (2PFM) the stress field near the crack tip is expressed by means of two parameters, i.e., the stress-intensity factor, *K*, and the *T*-stress. The stress field at the crack tip can then be expressed for a normal mode (mode I) of loading as

$$\sigma_{ij} = \frac{K_1}{\sqrt{2\pi r}} f_{ij}(\theta) + T\delta_{1i}\delta_{1j} \quad (1)$$

where $f_{ij}(\theta)$ is a known function of the polar angle θ, and δ_{ij} and δ_{1j} are the Cronecker deltas, taking the value 1 if i and j are equal, and 1 and 0 otherwise.

The work reported here uses 2PFM for a description of the different threshold values of a FCPR to predict the effect of constraint on the retardation or acceleration of the crack growth in high cyclic fatigue loading. The corresponding calculations are performed according to the finite-element method (FEM). The experimental measurements of FCPR on two kinds of specimens with a different geometries were compared and so were the experimental data covering the effect of constraint.

2 TESTS OF THE FATIGUE-CRACK PROPAGATION RATE NEAR TRESHOLD VALUES

The effect of constraint on the fatigue-crack growth rate near the threshold values was experimentally studied in relation to two different specimens: the M(T) (the middle-tension specimen) and C(T) (the compact-tension specimen). The M(T) specimen produced a low level of constraint (negative values of the *T*-stress) and the C(T) specimen produced a high level of constraint (positive

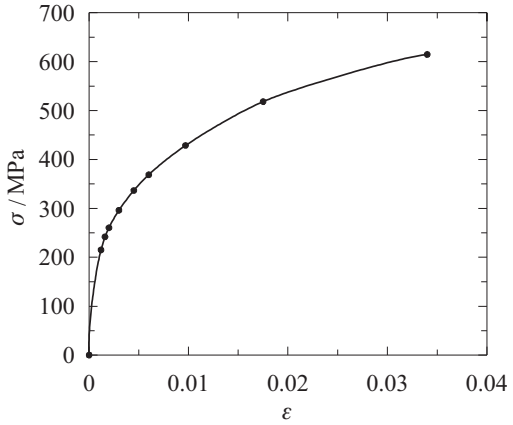

Figure 1: Cyclic stress-strain curve of the material used for experiments
Slika 1: Ciklična napetost-deformacija odvisnost materiala, ki je bil uporabljen za preizkuse

values of the *T*-stress) e.g., [6]. The thickness of both types of specimens was the same, B = 10 mm. The experimental results were obtained for steel with 0.45 % C. The material properties corresponding to the cyclic strain-stress curve (**Figure 1**) are: Young's modulus $E = 2.1 \cdot 10^5$ MPa, Poisson's ratio $\nu = 0.3$, cyclic yield stress $\sigma_0 = 350$ MPa and hardening exponent $n = 0.314$. All the experiments were performed under the same conditions: room temperature and a loading stress ratio $R \approx 0$ (close to a pulsating cycle $R = 0.1$). The crack length was measured optically with a resolution of 0.01 mm. The experimental data were evaluated according to ASTM E647[7]. The threshold values were determined at crack-growth rates of 10^{-8} mm/cycle.

The following results were obtained, see **Figure 2**. The fatigue-crack growth rate was found to be higher for the M(T) specimen with a negative value of *T*-stress (low constraint) than for the C(T) specimen with a positive value of *T*-stress (high constraint), when subjected to the same nominal range of the stress-intensity

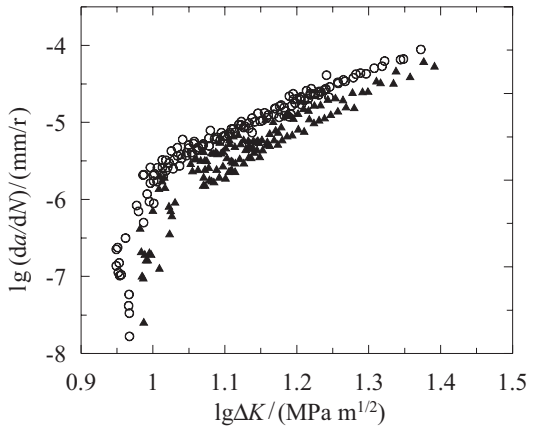

Figure 2: The influence of the geometry of the specimen on the threshold values and the fatigue crack propagating rate
Slika 2: Vpliv geometrije preizkušanca na vrednosti praga in hitrost propagacije utrujenostne razpoke

factor, ΔK. Significant differences were seen between the threshold values of the FCPR. The corresponding parameters of the Paris-Erdogan law are then: $C = 6.607 \cdot 10^{-11}$, $m = 4.609$ and $K_{th} = 8.81$ MPa m$^{1/2}$ for the M(T) specimen and $C = 2.883 \cdot 10^{-10}$, $m = 3.662$ and $K_{th} = 9.66$ MPa m$^{1/2}$ for the C(T) specimen.

3 CONSTRAINT-BASED DESCRIPTION OF A FATIGUE CRACK

The plastic-zone size around the crack tip depends upon many variables, such as the yield stress, the applied stress, the specimen geometry and the crack geometry. According to one-parameter linear-elastic fracture mechanics (LEFM), there is a single-valued relation between the size of the plastic zone and the corresponding value of the stress-intensity factor, K_I, which controls the FCPR (e.g.,[8]). Following this, one of the parameters, say $R_p = R_p(K)$, which characterizes the size of the plastic zone, can be used as the controlling variable, and the Paris-Erdogan law[9] $da/dN = C(K)^m$ can be rewritten in the form

$$\frac{da}{dN} = F\left[R_p(K)\right] \tag{2}$$

Therefore, the size of the plastic zone can be considered as a potential parameter with a direct physical meaning to describe the FCGR. Based on the assumptions of the 2PFM, the size of the plastic zone depends on the given value of K and the *T*-stress (the level of constraint), $R_p^* = R_p^*(K,T)$, and Equation (2) takes the form:

$$\frac{da}{dN} = F\left[R_p^*(K)\right] \tag{3}$$

Equation (3) considers the effect of the stress field at the crack tip on the FCPR, which included the non-singular term (*T*-stress), and this Equation (3) can be used to quantify the effect of the constraint.

In the present study, see e.g.[3], the plastic-zone area, $S_p(K,T)$, is used as a parameter controlling the FCPR, and it is assumed that the crack will propagate at the same fatigue rate if the values of $S_p(K,T)$ (corresponding to different combinations of the K and T parameters) are the same.

Let us take the level of constraint corresponding to the zero value of the *T*-stress as a reference state and denote the corresponding area of the plastic zone as $S_p^0 = S_p(K,T = 0)$, based on the assumption of LEFM it is

$$S_p^0 = S_p(K,T = 0) = \psi(\nu,T = 0)(K/\sigma_0)^4 \tag{4}$$

where $\psi(\nu,T = 0)$ is a function of Poisson's ratio, ν, and the cyclic yield stress, σ_0 of the material used. The function can be determined conventionally by substituting the singular terms of the elastic stress field into the von Mises' yield criterion or numerically using the FEM. Similarly, let us denote the area of the plastic zone around the crack tip corresponding to a structure

with a non-zero level of constraint as $S_p = S_p(K,T \neq 0)$, and express it in the form

$$S_p(K,T \neq 0) = \psi(\nu,T \neq 0)(K/\sigma_0)^4 \quad (5)$$

Both quantities, $\psi(\nu,T = 0)$ and $\psi(\nu,T \neq 0)$, were calculated numerically by using a modified boundary-layer analysis (MBLA). The calculations of the plastic-zone size and area were performed for different values of the stress-intensity factor as a function of the ratio of the T-stress and the yield stress, T/σ_0, in an interval of a real ratio < –0.8; 0.4 > (see also[10]). The chosen values of the K factor and the ratio T/σ_0 correspond to the applied levels of the external stress and the constraint in the presented experiments. The dependence obtained can then be expressed in the form

$$\lambda\left(\frac{T}{\sigma_0}\right) = 1 - 0.33\left(\frac{T}{\sigma_0}\right) + 0.66\left(\frac{T}{\sigma_0}\right)^2 - 0.445\left(\frac{T}{\sigma_0}\right)^3,$$

see **Figure 3**.

The relation between the plastic-zone sizes with and without using the T-stress was found in the form:

$$S_p(K,T) = \lambda^4(T/\sigma_0)S_p^{\,0} \quad (6)$$

Let us further define the effective value of the stress-intensity factor, K^{eff}, using the equality (6) that relates the plastic-zone area for $T = 0$ and $T \neq 0$ in the form:

$$K^{eff}(T) = \lambda(T/\sigma_0)K(T = 0) \quad (7)$$

Where the application of the $K^{eff}(T)$ for the description of the fatigue-crack growth rate takes the level of the applied stress and the constraint into account, the Paris-Erdogan equation can be rewritten in the form

$$da/dN = C[\lambda(T/\sigma_0)K]^m \quad (8)$$

Equation (8) represents a modified form of the Paris-Erdogan law and makes it possible to account for the effect of the constraint on the fatigue-crack growth rate. C and m are material constants obtained for conditions corresponding to $T = 0$. The value of the T-stress represents the level of constraint corresponding to the given specimen geometry.

4 DISCUSSION

The approach presented is a phenomenological one and does not consider the effect of plasticity-induced crack closure; it proceeds from the assumption of LEFM. The two-parameter fracture methodology is based upon the assumption that the fracture behaviour of two different bodies is the same if both encompass the same value of the stress-intensity factor, K, and the same range of the constraint parameter T-stress. Note that the positive values of the T-stress correspond to a high constraint level and negative values to a low constraint. The two-parameter description characterized the stress state near the crack tip more accurately, and can explain the effect of the outer geometry of the structure. On the other hand, this approach does not take account of the corresponding mechanism of the fatigue-crack growth rate or the microstructure of the material.

The correlation of the dependence $da/dN - K$ related to a zero constraint level for the steel specimens is shown in **Figure 4**. The corresponding Paris-Erdogan law parameters are $C = 1.473 \cdot 10^{-10}$, $m = 4.013$ and $K_{th} = 9.44$ MPa m$^{1/2}$. The points corresponding to the lower level of constraint (M(T) specimen) are shifted to lower values of the FCPR. Similarly, the points corresponding to a higher level of constraint (the C(T) specimen) are transformed into higher values of the FCPR. The scatter of the experimental results after this transformation is smaller in comparison to the data in **Figure 2**. Finally, it is possible to make an approximation of all experimental data by the one material curve, which is independent of the outer geometry of the specimen, with reasonable experimental scatter corresponding to a zero value of the constraint.

Similarly, the influence of the constraint can be described in the threshold region, see **Figure 4**.

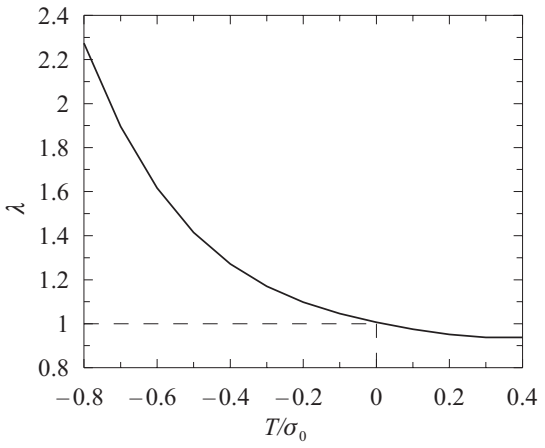

Figure 3: Dependence $\lambda = \lambda(T/\sigma_0)$
Slika 3: Odvisnost $\lambda = \lambda(T/\sigma_0)$

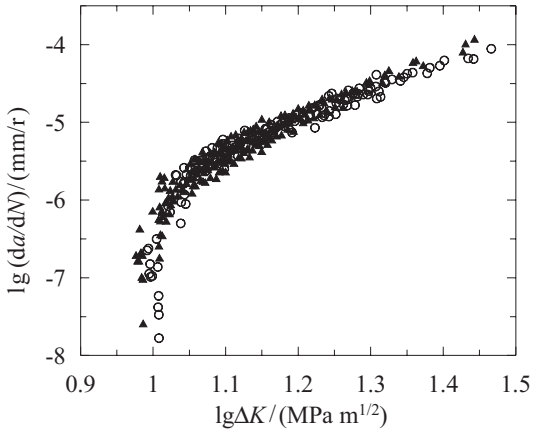

Figure 4: The experimental data from **Figure 2** correlated to a zero value of the constraint
Slika 4: Eksperimentalne vrednosti s **slike 2** korelirane na nično vrednost vpetosti

Following these observations it can be concluded that the fatigue crack will not propagate if the threshold value for zero T-stress is smaller than the effective range of the stress-intensity factor.

$$K^{\text{eff}}(K,T) < K_{\text{th}}(T = 0) \quad (9)$$

5 CONCLUSIONS

This work describes the constraint effect for fatigue-crack propagation near the threshold values in the context of the requirement for improved life-prediction methods. A combined experimental and modeling approach is used. Experimental measurements of the FCPR were made on two kinds of specimens with different shapes: i.e., M(T) (low level of constraint) and C(T) (high level of constraint) specimens.

The plastic zone is considered as a controlling variable for near-threshold fatigue-crack behaviour and a simple procedure makes it possible to estimate the changes of the fatigue-crack propagation rate in the threshold region due to different constraint levels formulated quantitatively.

The effective stress-intensity factor, K^{eff}, becomes smaller ($T > 0$) or larger ($T < 0$) than the nominally applied one, and hence the crack propagation is slower or faster, and the threshold values are lower or higher, *than would be predicted without any knowledge of the constraint effect*.

ACKNOWLEDGEMENT

This investigation was supported by grants No. 101/04/P001 of the Grant Agency of the Czech Republic and by the Institutional Research Plan AV OZ 204 105 07.

6 REFERENCES

[1] M. L. Williams: On the stress distribution at the base of a stationary crack. ASME Journal Applied Mechanics, 24 (**1957**), 109–123

[2] R. S. Vecchio, J. S. Crompton, R. W. Hartyberg: The influence of specimen geometry on near threshold fatigue crack growth, Fatigue Fracture Engineering Mat. Structure, 10 (**1987**), 333–342

[3] Z. Knesl, K. Bednar, J. C. Radon: Influence of T-stress on the rate of propagation of fatigue crack, Physical Mesomechanics, (**2000**), 5–9

[4] J. Tong: T-stress and its implications for crack growth, Engineering Fracture Mechanics, 69 (**2002**), 1325–1337

[5] J. A. Joyce: Evaluation of the Effect of Crack Tip Constraint on Fatigue Crack Growth Rate in Inconel 718, Fatigue and Fracture Mechanics: 34 (**2004**), ASTM STP 1461

[6] Z. Knesl, K. Bednar: Two-parameters Fracture Mechanics: Calculation of Parameters and their Values, Institute of Physics of Materials, Brno, Czech Republic, 1998

[7] ASTM E647-05 Standard Test Method for Measurement of Fatigue Crack Growth Rate. Vol. 03.01, 591–630

[8] S. Suresh: Fatigue of Materials, Cambridge University Press, Cambridge 1998

[9] P. Paris, F. Erdogan: A critical analysis of crack propagation laws, Journal Basic Engineering Trans. ASME, (**1963**), 528–534

[10] S. Seitl, P. Hutař: Influence of materials parameters on polynom used for modification Paris law, 22nd conference with international participation, Hrad Nečtiny, 2 (**2006**), 543–550, Text in Czech

UDC/UDK 669.18
Original scientific article/Izvirni znanstveni članek

ISSN 1580-2949
MTAEC9, 41(3)139(2007)

MODELLING OF THE SOLIDIFICATION PROCESS AND THE CHEMICAL HETEROGENEITY OF A 26NiCrMoV115 STEEL INGOT

MODELIRANJE PROCESA STRJEVANJA IN KEMIČNE HETEROGENOSTI INGOTA IZ JEKLA 26NiCrMoV115

Martin Balcar[1], Rudolf Železný[1], Ludvík Martínek[1], Pavel Fila[1], Jiří Bažan[2]

[1]ŽĎAS, a. s., Strojírenská 6, 591 71 Žďár nad Sázavou, Czech Republic
[2]University VŠB – TU Ostrava, FMMI, 17. listopadu 15, 708 33 Ostrava, Czech Republic
martin.balcar@zdas.cz

Prejem rokopisa – received: 2006-08-29; sprejem za objavo – accepted for publication: 2006-12-12

Steel making at ŽĎAS, a.s. using secondary metallurgy technology makes it possible to produce liquid metal with high levels of metallurgical cleanliness. During the casting and subsequent cooling of forging ingots, the steel solidification takes place. Directional material solidification, grain size, chemical heterogeneity and discontinuities can have a negative effect on the products' final properties. The comparison of the chemical composition based on a numerical calculation with the heterogeneity of the real ingot has proven the possibility of using MAGMA software to model the casting and solidification of ingots for open-die forgings made from 26NiCrMoV115 steel.

Key words: forging ingot, solidification, heterogeneity, modelling of segregations

Za uporabo tehnologije sekundarne metalurgije se v ŽĎAS izdeluje tekoče jeklo z veliko metalurško čistostjo. Med ulivanjem in ohlajanjem kovaških ingotov se izvrši strjevanje. Usmerjeno strjevanje, velikost zrn, kemična heterogenost in diskontinuitete lahko negativno vplivajo na lastnosti končnega proizvoda. Primerjava kemične sestave z numeričnim izračunom heterogenosti realnega ingota je dokazala možnost uporabe softvera MAGMA za modeliranje ulivanja in strjevanja ingotov za prosto kovanje iz jekla 26NiCrMoV115.

Ključne besede: kovaški ingot, strjevanje, heterogenost, modeliranje segregacij

1 INTRODUCTION

The manufacture of steel forgings for the rotary parts of gas turbines requires an adherence to exactly defined forming and heat-treatment rules. A prerequisite for the successful production of highly stressed machine parts is a high-quality initial blank or ingot.

The use of MAGMA software to model the ingot casting and solidification, to forecast the internal quality and the segregation of basic alloying elements and to compare the theoretical prerequisites with practical results makes it possible to evaluate the possibility of also using software for other types of numerical simulation related to the processing of ingots.

The evaluation of the chemical heterogeneity of the forging ingot of type 8K8.4 cast at ŽĎAS, a.s. from 26NiCrMoV115 steel demonstrated the requirements for an isotropic structure and mechanical properties of the steel forging are met.

2 MODELLING OF THE INGOT CASTING AND THE SOLIDIFICATION PROCESS

Using the MAGMA software a simulation of the casting and solidification of the 8K8.4 forging ingot in 30NiCrMoV steel with the chemical composition shown in **Table 1** was carried out.

The results of the numerical modelling of the ingot solidification process in the form of the location of the solidus temperature for different solidification times are shown in **Figure 1**. A graphical visualisation of the time

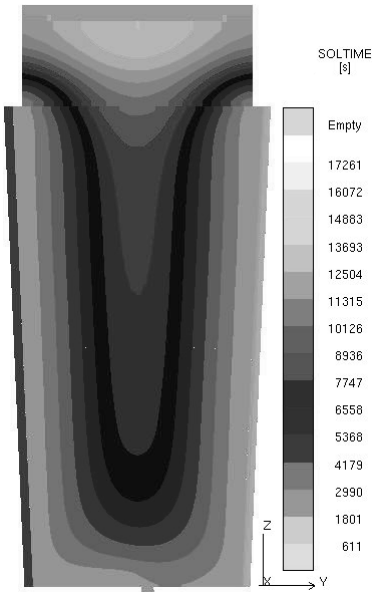

Figure 1: Development of the solidus temperature range depending on time
Slika 1: Časovna evolucija razpona solidusne temperature

Table 1: Chemical composition of steel as per the MAGMA software
Tabela 1: Kemična sestava jekla za softver MAGMA

MAGMA	C	Mn	Si	P	S	Cr	Ni	Cu	Mo	V	Al
	w/%										
30NiCrMoV	0.30	–	–	0.025	0.006	1.40	3.00	–	0.40	–	–

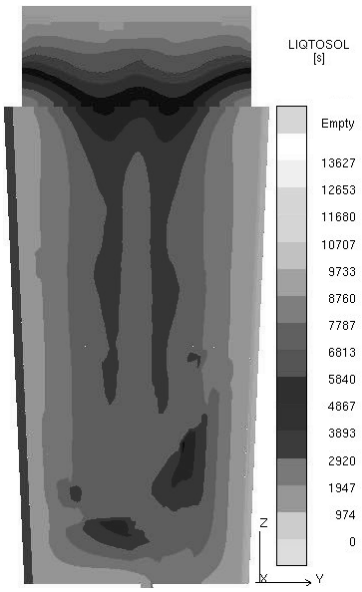

Figure 2: Stay of the melt in the phase boundary between the liquidus and solidus temperatures
Slika 2: Zadržanje taline na fazni meji med likvidusno in solidusno temperaturo

zones when the temperature of the molten steel changes through the phase between the liquidus and solidus lines is shown in **Figure 2**.

The final phase of the solidification process is intended for an immediate share of 100 % solid phase. [1]

Along with the numerical simulation of the ingot casting and the solidification, calculations of the segregation and unmixing of the basic alloying and tramp elements were also carried out. Significant concentration changes throughout the steel ingot's cross-section were only noted for elements with greater content. The concentration distribution of some elements is shown in **Figures 3 and 4**.

It is obvious that the degree of segregation increases from the ingot surface towards the axial part.

The concentration of the elements was deduced from the concentration ranges in **Figures 3 and 4** and arranged in an ascending order, with numbers from 0 to X, according to the local level of concentration. By summing the local content of all the elements the values in **Table 2** were obtained showing the relative segregation degree according to the location of the analyses points in **Figure 5**.

Table 2: Relative segregation degree
Tabela 2: Relativna stopnja segregacije

Sample	1	2	3
H	18	8	0
S	14	9	4
P	7	8	4

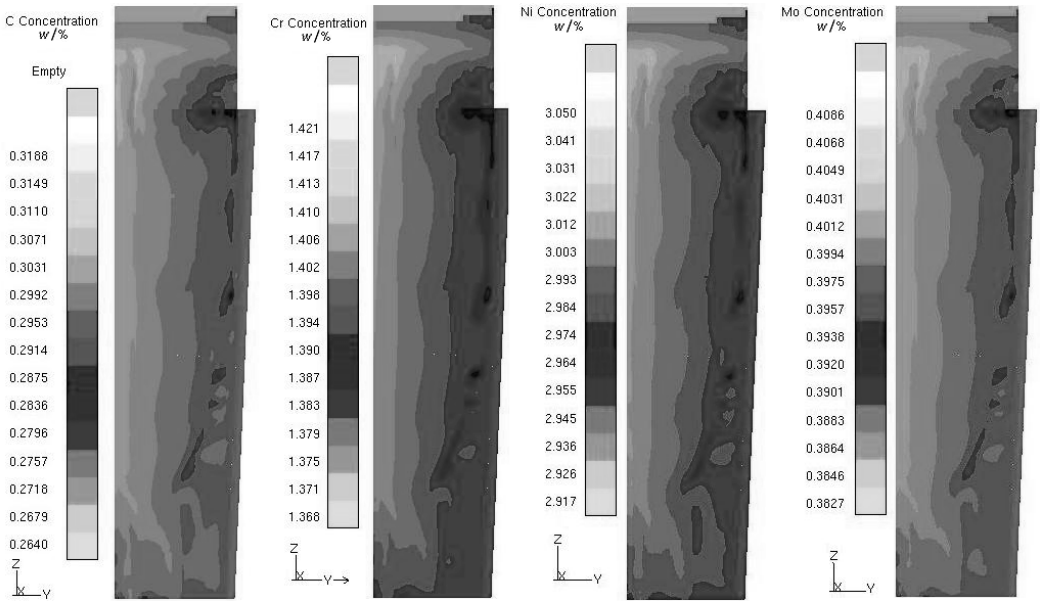

Figure 3: Concentration of some elements in the central vertical section of the ingot
Slika 3: Koncentracija nekaterih elementov na pokončnem prerezu skozi sredino ingota

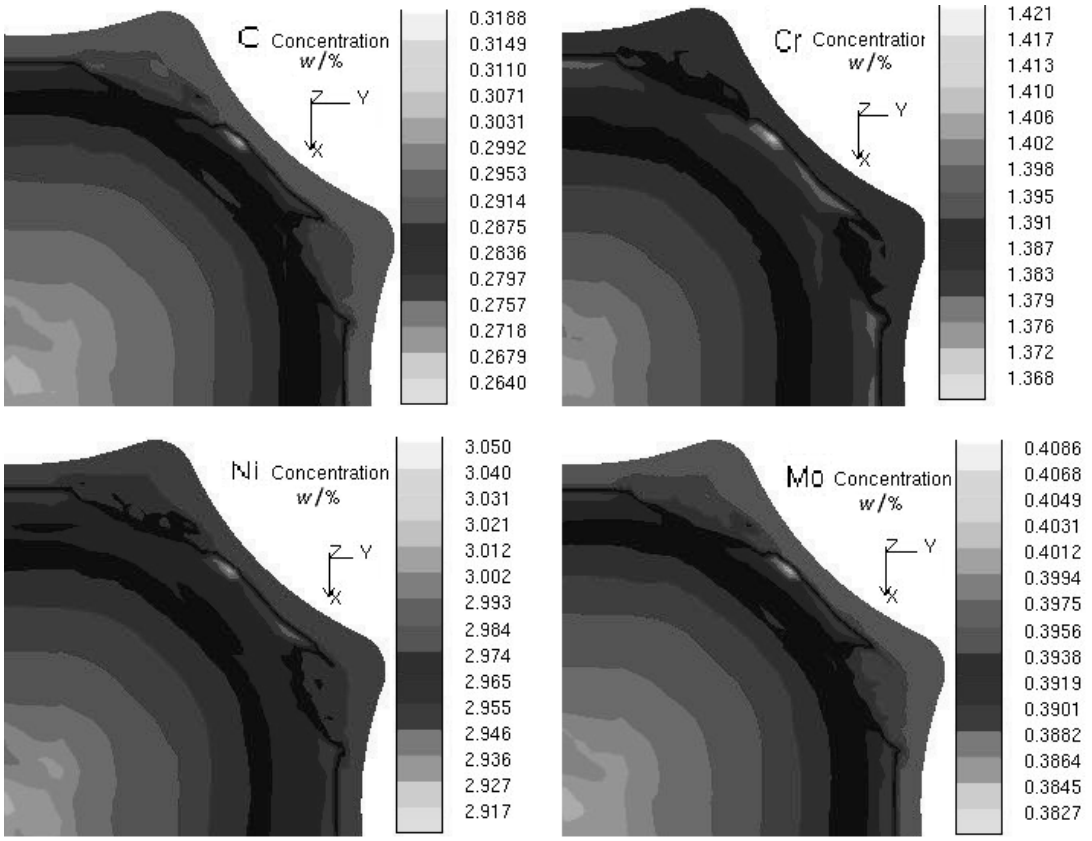

Cross-section view below the ingot top

Figure 4: Concentration of some elements in the cross-section, view below the ingot top
Slika 4: Koncentracija nekaterih elementov na prerezu pod glavo ingota

Table 3: Chemical composition of steel – final melt test
Tabela 3: Kemična sestava jekla, končna analiza šarže

Melt analyse	C	Mn	Si	P	S	Cr	Ni	Cu	Mo	V	Al	As	Sn	Sb	Ca
	w/%											µg/g			
30NiCrMoV	0.29	0.21	0.01	0.004	0.006	1.69	2.88	0.01	0.41	0.12	0.009	30	<5	<5	4

The highest values of the positive segregation correspond to the ingot part marked with the index H1. Compared with the other sampling points, all the elements attain the maximum concentration here.

The lowest concentrations of the analysed elements were found in H3 and events S3 and P3.

3 PRODUCTION PROCESSING AND SAMPLING METHOD

Within the scope of the experimental work, the 26NiCrMoV115 steel melt with the chemical composition in **Table 3** was made at ŽĎAS, a.s. The molten

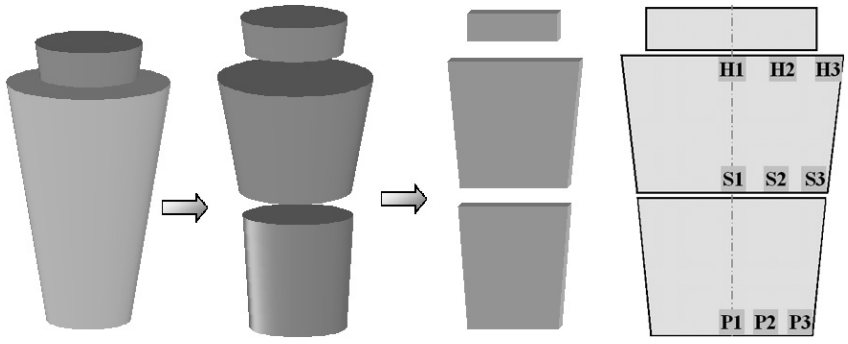

Figure 5: Steel ingot dividing and sampling diagram
Slika 5: Razdelitev ingota in skica odvzema vzorcev

metal was bottom cast in the mould of the 8K8.4 to form an ingot with a mass of approximately 8 tonnes. [3]

The solidification and the cooling of the ingot to ambient temperature took place in the mould. In order to facilitate the manipulation after the fettling, the ingot was divided into three parts using a cutting machine, as shown in **Figure 5**.

Figure 5 shows the sampling points for the specimens taken for analysis from parts below the top, from the middle and from the bottom of the ingot.

4 CHEMICAL COMPOSITION OF THE INGOT IN THE MONITORED ZONES

The samples H1, H2, H3 were cut out from the body part below the ingot top, the samples S1, S2, S3 from the middle part and the samples P1, P2 and P3 from the ingot's bottom part. All the samples were submitted for chemical analyses in the laboratory of ISPAT NOVÁ HUŤ, a.s. and the contents of several elements were determined. [4]

The chemical compositions of the samples, shown in **Table 4**, only include the elements present in sufficient concentrations with respect to the detection limits of the analytical device.

Table 4: Chemical composition of samples taken throughout the ingot cross-section
Tabela 4: Kemična analiza vzorcev, izrezanih iz prereza ingota

Sample	K	H1	H2	H3
C	0,29	0,315	0,292	0,294
Mn	0,21	0,21	0,20	0,20
P	0,004	0,004	0,005	0,004
S	0,006	0,006	0,005	0,006
Cr	1,69	1,67	1,63	1,63
Ni	2,88	2,88	2,80	2,83
Mo	0,41	0,449	0,381	0,405
V	0,12	0,127	0,111	0,117
Al	0,009	0,010	0,010	0,011

Sample	K	S1	S2	S3
C	0,29	0,298	0,289	0,290
Mn	0,21	0,20	0,20	0,20
P	0,004	0,003	0,004	0,004
S	0,006	0,005	0,007	0,006
Cr	1,69	1,62	1,63	1,63
Ni	2,88	2,77	2,82	2,80
Mo	0,41	0,381	0,398	0,396
V	0,12	0,111	0,116	0,116
Al	0,009	0,010	0,010	0,011

Sample	K	P1	P2	P3
C	0,29	0,289	0,289	0,282
Mn	0,21	0,20	0,20	0,20
P	0,004	0,004	0,005	0,004
S	0,006	0,006	0,006	0,006
Cr	1,69	1,62	1,64	1,61
Ni	2,88	2,82	2,83	2,77
Mo	0,41	0,403	0,415	0,409
V	0,12	0,116	0,121	0,117
Al	0,009	0,010	0,010	0,010

If the concentrations of the elements from **Table 4** are arranged in ascending order, with evaluation points from 0 to X according to the increasing content, a sum for all the elements indicating the relative segregation degree in **Table 5** is obtained.

Table 5: Relative segregation degree
Tabela 5: Relativna stopnja segregacije

Sample	1	2	3
H	27	8	18
S	7	11	9
P	10	19	9

In the zone corresponding to the ingot part marked with H1 the highest positive segregations occur. In this area most elements show a significant unmixing. Compared with other sampling points, carbon, chromium, nickel, molybdenum and vanadium attain the maximum segregation; the lowest concentrations of the elements analysed were found in the S1 and also in the S3 and P3 zones.

5 ELEMENT HETEROGENEITY MEASUREMENT

The chemical heterogeneity of the steel samples was determined at VTÚO Brno using a method previously reported [5]. For the energy-dispersion (ED) X-ray microanalysis a JEOL JXA8600/KEVEX Delta V Sesame microscope was used.

The analyses were performed for elements with a content higher than the detection limit for the ED microanalysis. For each analysed element the content was determined for 101 points. The analysed elements were vanadium, chromium, manganese, iron, nickel and molybdenum.

For each point analyses, the program also determined some basic statistical parameters:

X_S mean value
S_X standard deviation
Min minimum value
I_{Het} heterogeneity index $I_{Het} = S_X/X_S$
Max maximum value
I_s segregation index $I_s = Max/X_S$

The results are shown in **Table 6**. For the evaluation of the chemical heterogeneity the maximum point content for each element was considered and obtained along a measured line of 1000 μm for each sample.

The dimensionless parameter known as the segregation index (I_s) was determined as the relationship between the maximum concentration and the average concentration in the given section ($I_s = Max/X_S$). The results are shown in **Table 7**.

Table 6: Basic statistics of samples and elements
Tabela 6: Osnovna statistika vzorcev in elementov

H	H1				H2				H3			
	XS	SX	Min	Max	XS	SX	Min	Max	XS	SX	Min	Max
V	0.096	0.077	0.000	0.593	0.065	0.044	0.000	0.173	0.066	0.052	0.000	0.223
Cr	1.723	0.447	0.959	3.119	1.535	0.370	0.939	3.079	1.464	0.287	0.929	2.269
Mn	0.085	0.095	0.000	0.360	0.146	0.105	0.000	0.400	0.080	0.084	0.000	0.370
Fe	94.72	0.84	91.48	96.31	95.33	0.56	93.82	96.50	95.34	0.48	94.02	96.37
Ni	2.967	0.305	2.301	3.791	2.683	0.269	2.091	3.331	2.865	0.274	2.031	3.611
Mo	0.406	0.269	0.037	1.687	0.239	0.135	0.000	0.667	0.185	0.106	0.000	0.547
S	**S1**				**S2**				**S3**			
	XS	SX	Min	Max	XS	SX	Min	Max	XS	SX	Min	Max
V	0.096	0.146	0.000	1.223	0.067	0.040	0.000	0.173	0.084	0.052	0.000	0.213
Cr	1.561	0.477	0.999	3.119	1.507	0.248	1.119	2.559	1.566	0.239	0.969	2.339
Mn	0.114	0.096	0.000	0.360	0.087	0.089	0.000	0.380	0.147	0.115	0.000	0.410
Fe	95.19	1.13	91.38	96.41	95.25	0.39	94.19	96.04	95.18	0.49	93.54	96.07
Ni	2.729	0.271	2.151	3.551	2.918	0.227	2.351	3.501	2.780	0.264	2.121	3.561
Mo	0.313	0.391	0.000	1.787	0.173	0.096	0.007	0.427	0.241	0.132	0.007	0.797
P	**P1**				**P2**				**P3**			
	XS	SX	Min	Max	XS	SX	Min	Max	XS	SX	Min	Max
V	0.108	0.076	0.000	0.343	0.085	0.048	0.000	0.193	0.071	0.050	0.000	0.213
Cr	1.693	0.481	1.049	3.579	1.603	0.577	1.079	5.129	1.499	0.451	0.829	3.129
Mn	0.221	0.129	0.000	0.480	0.242	0.137	0.000	0.530	0.095	0.083	0.000	0.330
Fe	94.79	0.92	90.42	96.26	95.18	0.70	91.05	96.18	95.26	0.59	93.68	96.31
Ni	2.824	0.283	2.151	3.441	2.688	0.250	2.111	3.261	2.851	0.270	2.331	3.451
Mo	0.370	0.380	0.000	3.147	0.202	0.113	0.017	0.847	0.226	0.140	0.000	0.647

Table 7: I_{Het} and I_s indexes
Tabela 7: Indeks I_{Het} in I_s

H	H1		H2		H3	
	I_{Het}	I_s	I_{Het}	I_s	I_{Het}	I_s
V	0.802	**6.177**	0.677	**2.662**	0.788	**3.379**
Cr	0.259	**1.810**	0.241	**2.006**	0.196	**1.550**
Mn	1.118	**4.235**	0.719	**2.740**	1.050	**4.625**
Fe	0.009	**1.017**	0.006	**1.012**	0.005	**1.011**
Ni	0.103	**1.278**	0.100	**1.242**	0.096	**1.260**
Mo	0.663	**4.155**	0.565	**2.791**	0.573	**2.957**
S	**S1**		**S2**		**S3**	
	I_{Het}	I_s	I_{Het}	I_s	I_{Het}	I_s
V	1.521	**12.740**	0.597	**2.582**	0.619	**2.536**
Cr	0.306	**1.998**	0.165	**1.698**	0.153	**1.494**
Mn	0.842	**3.158**	1.023	**4.368**	0.782	**2.789**
Fe	0.012	**1.013**	0.004	**1.008**	0.005	**1.009**
Ni	0.099	**1.301**	0.078	**1.200**	0.095	**1.281**
Mo	1.249	**5.709**	0.555	**2.468**	0.548	**3.307**
P	**P1**		**P2**		**P3**	
	I_{Het}	I_s	I_{Het}	I_s	I_{Het}	I_s
V	0.704	**3.176**	0.565	**2.271**	0.704	**3.000**
Cr	0.284	**2.114**	0.360	**3.200**	0.301	**2.087**
Mn	0.584	**2.172**	0.566	**2.190**	0.874	**3.474**
Fe	0.010	**1.016**	0.007	**1.011**	0.006	**1.011**
Ni	0.100	**1.218**	0.093	**1.213**	0.095	**1.210**
Mo	1.027	**8.505**	0.559	**4.193**	0.619	**2.863**

Table 8: Maximum and minimum segregation indexes
Tabela 8: Največji in najmanjši indeksi segregacije

Maximal and minimal segregation idexes

H1	H2	H3
S1	S2	S3
P1	P2	P3

	V	
6.18	2.66	3.38
12.74	2.58	2.54
3.18	2.27	3.00

	Mn	
4.24	2.74	4.63
3.16	4.37	2.79
2.17	2.19	3.47

	Ni	
1.28	1.24	1.26
1.30	1.20	1.28
1.22	1.21	1.21

	Cr	
1.81	2.01	1.55
2.00	1.70	1.49
2.11	3.20	2.09

	Fe	
1.02	1.01	1.01
1.01	1.01	1.01
1.02	1.01	1.01

	Mo	
4.16	2.79	2.96
5.71	2.47	3.31
8.51	4.19	2.86

Table 9: Mass distribution of segregation indexes
Tabela 9: Razdelitev indeksov segregacije po masi

Maxima				Minima		
H1	H2	H3		H1	H2	H3
S1	S2	S3		S1	S2	S3
P1	P2	P3		P1	P2	P3
1	0	1		0	0	0
2	0	0		0	3	1
1	1	0		1	1	0

In order to make it easier to understand, the segregation index for the analysed elements is arranged so that it emphasizes the maximum and minimum segregation index. According to the position of the samples in the ingot, the following indexes were determined.

The distribution of the values of the maximum and minimum segregation indexes of the elements shows that it is not possible to decide unambiguously in which ingot part the highest and/or lowest segregation intensity occurs.

If we assign the same weight to the highest and/or the lowest segregation index of each element (six analysed elements with a mass of 1/6), the distribution of the maximum and/or minimum segregation indexes of the elements, the data in **Table 8**, are obtained.

Table 10: Limit values of the segregation indexes related to the elements
Tabela 10: Mejne vrednosti za indekse segregacije za elemente

Maxima		
H1	H2	H3
S1	S2	S3
P1	P2	P3
Fe		Mn
V Ni		
Mo	Cr	

Minima		
H1	H2	H3
S1	S2	S3
P1	P2	P3
	Fe Ni Mo	Cr
Mn	V	

These data show that the highest segregation index is obtained in the ingot axis area, where a fraction of 4/6 of cases falls on the vertical column of samples H1-S1-P1

The smallest segregation index is found for samples from the S2 ingot position. In terms of the fraction 3/6 it means S2 takes half of all cases. The fraction 2/3 of cases falls on the column H2, S2 and P2.

The minimum fraction 1/6 of the lowest measured values of the segregation indexes falls on the vertical columns H1–S1–P1 and H3–S3–P3, while in the column H1–S1–P1 the weight of occurrence of the elements with the maximum heterogeneity index is 2/3. It can be concluded that the highest unmixing tendency is expected in the ingot axis – column 1. The lowest unmixing tendency can be expected at the surface of the ingot – column 3.

The segregation behaviour of the elements Cr and Mn is different, as shown in **Table 9**.

The smallest measured segregation indexes are found for the ingot areas H2, S2 and P2. However, there are also two exceptions to this rule, again the elements are Cr and Mn.

Sequence according to the highest segregation index:

Table 11: Sequence of segregation indexes
Tabela 11: Sekvence indeksov segregacije

Segregation	V	Mo	Mn	Cr	Ni	Fe
Index	12.74	8.51	4.63	3.20	1.30	1.02

Sequence of elements according to the lowest segregation index:

Segrgeation	Mo	V	Mn	Cr	Ni	Fe
Index	2.47	2.27	2.17	1.49	1.20	1.01

Both sequences are almost identical, i.e., Mo, V, Mn, Cr, Ni and Fe and only two elements, molybdenum and vanadium, exchange their places in the sequence.

In both sequences the elements V, Mo and Mn are in the first three places and the sequence is ended by the elements Cr, Ni and Fe. The reciprocal value of the segregation index $k \approx 1/I_s$ represents, as a first approximation, the effective distribution coefficient of the element [6].

6 CONCLUSION

The relatively good agreement of the results of the measurements and the simulations of the maximum and minimum segregation index sequence indicate the same tendencies during the solidification and cooling of a steel ingot with a given chemical composition.

On the basis of the measurements it can be concluded that this tendency depends on the real value of the effective distribution coefficient of the elements. It is also possible to conclude on the basis of the measurements that, of the external parameters, the parameter referred to as the local solidification time plays an important role, i.e., the time when the particular measured area of the sample stays between the solidus and liquidus temperatures.

The use of the MAGMA software to model the ingot casting and solidification process and to predict the behaviour of the basic alloying elements confirms the relative agreement between the theoretical predictions and the practical results.

The determination of the chemical heterogeneity of the forging ingot type 8K8.4 of 26NiCrMoV115 steel will contribute to an explanation of the causes of possible occurrence of structural anisotropy of the steel in connection with the end-use properties.

ACKNOWLEDGEMENTS

The investigations were performed within the EUREKA programme of the E!3192 ENSTEEL project, identification number 1P04EO169. The project was funded partially with the financial support of the Ministry of Education, Youth and Sport of the Czech Republic

7 LITERATURE

[1] Martínek, L., Balcar, M., Bažan, J. et al.: Optimization of casting and solidification with respect to the ingot structure and homogeneity. Progress report from the solution of the EUREKA E!3192 ENSTEEL project, identification number 1P04OE169, 2005, 69 p.

[2] Martínek, L., Balcar, M. Železný, R.: Optimization of casting and solidification with respect to the ingot structure and homogeneity. Annex No. 4: Numerical simulation outputs and selected quality parameters of the ingot. Progress report form the solution of the EUREKA E!3192 ENSTEEL project, identification number 1P04OE169, 2005, 97 p.

[3] Martínek, L., Balcar, M. et al.: Production of components from high-clean steels for power equipment. Progress report on the solution of the EUREKA E!3192 ENSTEEL project, 2004, 117 p.

[4] Metallurgical and chemical laboratories ISPAT NOVÁ HUŤ a.s., Test report, 2004

[5] Bažan, J. et al.: Comparison of influence of the contemporary, single and combined processes of extra-furnace metallurgy and casting on the end-use properties and expensiveness of high-grade steels. /Opposed final report of the grant project GAČR 106/01/0365/. VŠB - TU Ostrava, 2003, 68 p.

[6] Rek, A., Stránský, K.: Element heterogeneity in the 26NiCrMoV115 steel samples from the 8 t ingot. VTÚO Brno, 2004, 35 p.

UDK/UDC 621.5/.6:533.5
Izvirni znanstveni članek/Original scientific article

ISSN 1580-2949
MTAEC9, 41(3)145(2007)

FREKVENČNA ODVISNOST REZIDUALNEGA TRENJA VISKOZNOSTNEGA VAKUUMSKEGA MERILNIKA Z LEBDEČO KROGLICO

FREQUENCY DEPENDENCE OF SPINNING ROTOR GAUGE RESIDUAL DRAG

Janez Šetina

Inštitut za kovinske materiale in tehnologije, Lepi pot 11, 1000 Ljubljana, Slovenija
janez.setina@imt.si

Prejem rokopisa – received: 2007-04-18; sprejem za objavo – accepted for publication: 2007-05-07

Viskoznostni merilnik tlaka z lebdečo kroglico (SRG – Spinning Rotor Gauge) se je uveljavil v meroslovju nizkih tlakov kot precizen in stabilen referenčni etalon za območje med 10^{-4} Pa in 1 Pa. Ob ustrezni kalibraciji s primarnimi vakuumskimi standardi je v tem območju tlakov dosegljiva merilna negotovost pri komercialnih merilnikih ± 0,5 %. Med vplivnimi veličinami pri merjenjih z SRG-merilnikom je najpomembnejše rezidualno trenje rotorja, ki se pojavi zaradi vrtinčnih električnih izgub pri magnetnem lebdenju in vrtenju kroglice. Rezidualno trenje lahko izmerimo pri zelo nizkem tlaku kot ničelni signal in ga nato upoštevamo pri meritvi tlaka kot popravek. Časovna stabilnost rezidualnega trenja določa spodnjo merilno mejo SRG-merilnika. Izkaže se, da je rezidualno trenje odvisno od frekvence vrtenja rotorja. Frekvenčno odvisnost lahko določimo z linearno regresijo merjenih vrednosti rezidualnega trenja v odvisnosti od frekvence. Podrobneje smo raziskali stabilnost in frekvenčno odvisnost rezidualnega trenja pri različnih namestitvah dveh kroglic. Rezultati so pokazali, da je frekvenčna odvisnost slabo korelirana z absolutno vrednostjo rezidualnega trenja. V večini primerov je frekvenčna odvisnost tako velika, da jo moramo upoštevati pri izračunu popravka rezidualnega trenja pri meritvah tlakov plina pod $1 \cdot 10^{-3}$ Pa.

Ključne besede: viskoznostni vakuumski merilnik, rezidualno trenje, meritev vakuuma

Spinning rotor gauge (SRG) is well recognized in the field of low pressure metrology as precise and stable reference standard in the range from 10^{-4} Pa to 1 Pa. The achievable measurement uncertainty of commercial SRG is ± 0,5%, assuring a suitable calibration with a higher level primary standard. Important correction of SRG is the pressure independent contribution to the measured signal known as residual drag. It is caused by eddy current losses in magnetic levitation system and metallic parts in the close vicinity of the spinning rotor, and can be determined at very low gas pressure as a zero signal of the gauge. The residual drag usually depends on the rotational frequency of the rotor. It can be approximated with a linear function which can be determined by linear regression of measured values as a function of rotational frequency. We have investigated stability and frequency dependence of residual drag for several different suspensions of two SRG rotors. Results showed that there is no correlation between frequency dependence and magnitude of residual drag. The frequency dependence is in most cases large enough to have significant influence on the measurements and has to be taken into account for precise pressure measurements below $1 \cdot 10^{-3}$ Pa.

Key words: spinning rotor gauge, residual drag, vacuum measurement

1 UVOD

Vsakršno gibanje predmetov v plinu je ovirano zaradi trkov z molekulami plina. Parameter, ki pove, kako močno je gibanje v nekem plinu ovirano, je viskoznost. Pojav molekularnega trenja je povezan s prenosom gibalne količine med molekulami plina in gibajočim predmetom. Enako kot toplotna prevodnost je tudi viskoznost plinov pri nizkem tlaku plina (v molekularnem področju) sorazmerna s tlakom, kar lahko izkoristimo za posredno merjenje vakuuma.

Shematski prerez viskoznostnega vakuumskega merilnika z lebdečo kroglico (angleško: SRG – Spinning Rotor Gauge) je prikazan na **sliki 1**. Merilni element je jeklena kroglica s premerom 4,5 mm, ki prosto lebdi v magnetnem ležaju [1]. Kroglica se nahaja v nekaj centimetrov dolgi cevki z notranjim premerom 8 mm. Cevka je z ene strani zaprta, z druge strani pa je privarjena v prirobnico, ki je povezana s posodo, v kateri merimo tlak plina. Merilna glava, ki zagotavlja magnetno lebdenje, pospeševanje in induktivno merjenje frekvence kroglice, se nahaja zunaj vakuuma. Kroglico pospešimo (z vrtečim se magnetnim poljem, podobno kot pri asinhronskem elektromotorju) do frekvence 400 Hz in nato pustimo, da se prosto vrti v razredčenem plinu. Trenje z molekulami plina kroglico zavira. Merjena veličina je časovna odvisnost kotne hitrosti kroglice ω. Z $\dot{\omega}$ označimo časovni

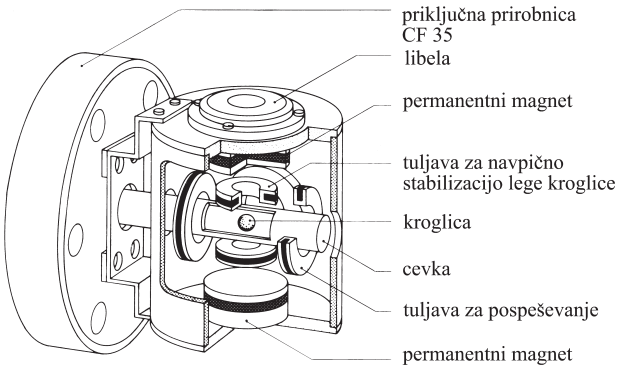

Slika 1: Prerez merilne glave SRG-merilnika
Figure 1: Cross section of a suspension head of SRG

odvod kotne hitrosti. Definirajmo relativni pojemek kotne hitrosti $(-\dot{\omega}/\omega)$, ki ga bomo zaradi lažjega pisanja v nadaljevanju označevali z *DCR* (okrajšava iz angleških besed ***Dec**eleration **R**ate*):

$$DCR = -\frac{\dot{\omega}}{\omega}$$

DCR je v molekularnem področju sorazmeren s tlakom plina [1]:

$$p = K_p \cdot DCR \qquad (1)$$

Sorazmernostni faktor K_p v **enačbi (1)** je konstanta občutljivosti SRG-merilnika:

$$K_p = \frac{a\rho}{10\sigma}\sqrt{\frac{8\pi RT}{M}} \qquad (2)$$

K_p vsebuje gostoto ρ in premer kroglice *a,* molekulsko maso *M* in temperaturo plina *T*, koeficient prenosa gibalne količine σ ter plinsko konstanto *R*. Edini parameter v **enačbi (2)**, ki ga ne moremo zanesljivo izmeriti ali napovedati je σ, zato ga moramo za izbrano kroglico in vrsto plina določiti s kalibracijo. V praksi se je izkazalo [2], da je za plin dušik na površini gladkih jeklenih kroglic σ med 0,94 in 1,06. Razlike med različnimi plini so v mejah ± 2 % [3,4].

SRG-merilnik je pomemben predvsem, ker v stabilnosti prekaša vse druge merilnike v visokovakuumskem področju. V različnih raziskavah so ugotovili, da se pri pazljivem ravnanju konstanta občutljivosti SRG-merilnika v daljšem časovnem obdobju (več let) običajno spremeni za manj kot 1 %. Merilnik se je v vakuumskem meroslovju uveljavil kot prenosni etalonski merilnik oziroma sekundarni referenčni merilnik [5]. V Laboratoriju za metrologijo tlaka na IMT je SRG-merilnik slovenski nacionalni etalon v območju med 10^{-5} Pa in 0,1 Pa [6]. Zaradi majhnega delovnega volumna in inertnosti je SRG merilnik še posebej primeren za meritve tlaka in netesnosti v majhnih hermetičnih sistemih [7,8,9].

2 REZIDUALNO TRENJE ROTORJA

Poleg molekularnega trenja pri SRG-merilniku opazimo tudi majhno, od tlaka in vrste plina povsem neodvisno zaviranje kroglice. To je tako imenovano rezidualno trenje, ki je navadno tako veliko, kot bi bilo trenje v plinu (dušiku) pri tlaku med 10^{-4} Pa in 10^{-2} Pa. Na prvi pogled se zdi, da zaradi rezidualnega trenja sploh ne moremo natančno meriti tlakov pod 10^{-2} Pa. Vendar lahko rezidualno trenje predhodno izmerimo tako, da sistem izčrpamo do tlaka pod $1 \cdot 10^{-6}$ Pa, ko postane molekularno trenje zanemarljivo v primeri z rezidualnim. Tedaj merilnik pokaže "ekvivalent tlaka", ki ustreza rezidualnemu trenju kroglice in ga navadno imenujemo "ofset" (*OFS*) oziroma ničelni premik:

$$OFS = K_p \cdot DCR_{p=0} \qquad (3)$$

Pri meritvi tlaka dobimo pravi tlak plina *p*, ki je posledica molekularnega trenja tako, da v **enačbi 1** od merjenega relativnega kotnega pospeška *DCR* odštejemo od tlaka neodvisni prispevek $DCR_{p=0}$:

$$p = K_p \cdot (DCR - DCR_{p=0}) = \Psi - OFS \qquad (4)$$

Tu je Ψ prikazana vrednost tlaka brez popravka rezidualnega trenja (osnovni signal). Če popravek rezidualnega trenja izražamo v enotah tlaka (*OFS*), moramo pri tem navesti, za katero vrsto plina velja, saj je sorazmernostni faktor K_p odvisen od molekularne mase plina. V nadaljevanju bomo vse vrednosti Ψ in *OFS* izražali v ekvivalentu tlaka dušika.

Rezidualno trenje izmerimo tako, da izčrpamo sistem s SRG-merilnikom do tlaka *p*, ki je nižji od negotovosti, ki jo želimo doseči, in lahko naredimo približek $OFS = \Psi$. Tako je za meritve v območju 10^{-1} Pa navadno dovolj, da izmerimo ničelni premik pri tlaku pod 10^{-4} Pa, kar je manj kot 0,1 % merjenega tlaka. Za precizijske meritve nizkih tlakov pod 10^{-3} Pa moramo ničelni premik izmeriti pri tlakih pod 10^{-6} Pa.

Običajen postopek za popravek rezidualnega trenja, ki ga priporoča proizvajalec [10] v svojih navodilih, je naslednji:

1. Izčrpati sistem pod mejo ločljivosti ($<10^{-6}$ Pa);
2. v kontrolni enoti nastaviti (resetirati) parameter *OFS* na vrednost 0;
3. aktivirati nov merilni cikel in izmeriti ničelni premik (prikazana vrednost pri tlaku plina $p \approx 0$), na primer $2{,}5678 \cdot 10^{-4}$ Pa;
4. izmerjeno vrednost vnesti v kontrolno enoto kot novo vrednost parametra $OFS = 2{,}5678 \cdot 10^{-4}$ Pa

Pri vseh nadaljnjih meritvah elektronska kontrolna enota avtomatično odšteva *OFS* od osnovne merjene vrednosti in tako prikaže tlak s popravkom rezidualnega trenja (**enačba 4**).

Rezidualno trenje nastopi zaradi več pojavov. Poglavitni vzrok rezidualnega trenja pri komercialnih SRG-merilnikih so inducirani vrtinčni tokovi [11]. Pri tem razlikujemo:

- vrtinčne tokove, ki se inducirajo v sami kroglici, če magnetno polje, v katerem lebdi kroglica, ni simetrično okrog osi vrtenja kroglice;
- vrtinčne tokove, ki se inducirajo v kovinskih delih v neposredni bližini kroglice zaradi vrteče se komponente magnetnega momenta kroglice (ta nam v detekcijskih tuljavah tudi inducira sinusni signal za merjenje kotne hitrosti).

Zaradi induciranih vrtinčnih tokov se kroglici zmanjšuje njena rotacijska energija, ki se pretvarja v električno delo oziroma toplotne izgube. Čeprav so te izgube znatne v primeri z molekularnim trenjem pri nizkih tlakih, je segrevanje kroglice in njene okolice zaradi njih prav neznatno. Moč, ki ustreza rezidualnemu ali molekularnemu trenju pri 10^{-3} Pa je namreč le 10^{-10} W.

V praksi se je izkazalo, da velikosti rezidualnega trenja za neko kroglico ne moremo vnaprej napovedati ali izračunati, saj je odvisna tako od asimetrije magnetnega polja, v katerem lebdi kroglica, kot tudi od velikosti

in smeri vrteče se komponente magnetnega momenta kroglice. Zato je rezidualno trenje za različne kroglice različno. Prav tako dobimo pri neki kroglici vsakič drugačno vrednost rezidualnega trenja, če kroglico vzamemo iz merilne glave in jo nato ponovno namestimo vanjo. Pri vsakem lebdenju se namreč kroglica drugače orientira v magnetnem polju. Poskusi, da bi stabilizirali orientacijo kroglice v magnetnem polju in s tem tudi rezidualno trenje, se niso obnesli [12]. Čeprav se rezidualno trenje ne vede ponovljivo, pa je na srečo pri večini kroglic stabilno, če merilnika ne izklopimo in s tem ne prekinemo lebdenja kroglice.

3 EKSPERIMENTALNO DELO

Pri meritvi z SRG-merilnikom je osnovni signal vedno vsota rezidualnega in molekularnega trenja. Po naših izkušnjah lahko zavzame rezidualno trenje širok obseg vrednosti od $5 \cdot 10^{-5}$ Pa do 10^{-2} Pa, a je najpogosteje v območju med $2 \cdot 10^{-4}$ Pa in $8 \cdot 10^{-4}$ Pa. Rezidualno trenje je najpomembnejši popravek pri SRG-merilniku v območju zelo nizkih tlakov. Negotovost popravka je odvisna od negotovosti, ki jo dosežemo pri merjenju rezidualnega trenja, in od kratkoročne oziroma dolgoročne stabilnosti. Ker ne moremo meriti hkrati tlaka plina in rezidualnega trenja, lahko negotovost ničelnega popravka v času meritve tlaka pravilno ocenimo le, če imamo dovolj podatkov o njegovi stabilnosti.

Pri našem eksperimentu smo SRG-merilnik izčrpali na ultravisokovakuumskem sistemu do tlaka pod $2 \cdot 10^{-7}$ Pa in z računalnikom neprekinjeno zapisovali frekvenco rotorja in prikazano vrednost tlaka Ψ brez popravka rezidualnega trenja. Meritev je trajala 4 dni. Pri integracijskem intervalu 30 s bi v tem času dobili več kot 10 000 prikazanih vrednosti, zato smo v programu za zajem podatkov uvedli povprečenje 10 zaporednih prikazanih vrednosti in v datoteko shranjevali povprečne vrednosti frekvence in tlaka v časovnem intervalu 300 s. S povprečenjem se je tudi zmanjšal statistični šum za faktor $\sqrt{10}$. V nadaljevanju eksperimenta smo izmerili frekvenčno odvisnost rezidualnega trenja pri večjem številu različnih namestitev dveh rotorjev.

V kontrolno enoto SRG-merilnika so bili pri vseh meritvah vneseni parametri za plin dušik pri temperaturi 293 K (**enačba 2**).

4 REZULTATI IN DISKUSIJA

A – Frekvenčna odvisnost in časovna stabilnost rezidualnega trenja

Primer neprekinjene meritve osnovnega signala Ψ pri tlaku pod $2 \cdot 10^{-7}$ Pa v časovnem obdobju 100 h je prikazan na **sliki 2 a**. Na **sliki 2 b** je prikazana tudi frekvenca rotorja, ki smo jo merili hkrati s Ψ. Na **sliki 2a** opazimo žagast potek signala, ki je koreliran s frekvenco

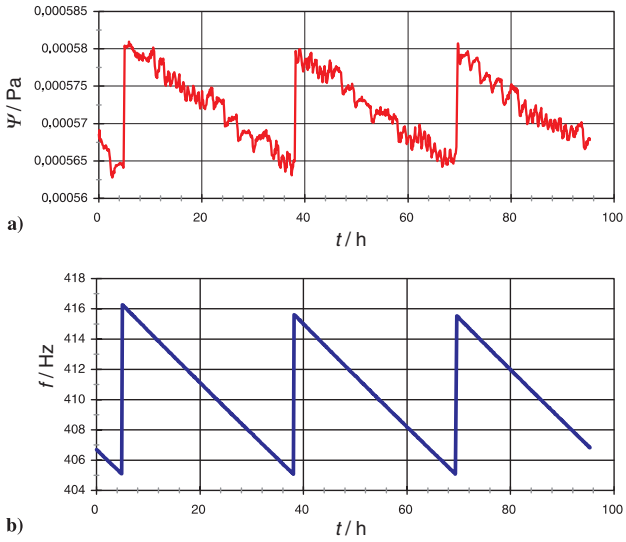

Slika 2: Prikazana vrednost SRG-merilnika (Ψ) v odvisnosti od časa (t) pri tlaku pod 10^{-6} Pa (a) in potek frekvence rotorja (f) v daljšem časovnem obdobju (b)

Figure 2: Displayed value of SRG (Ψ) versus time (t) at gas pressure below 10^{-6} Pa (a), and rotor frequency (f) (b)

rotorja. Žagast potek frekvence je povezan s samodejnim pospeševanjem rotorja. Ko pade frekvenca rotorja pod spodnjo mejo 405 Hz, elektronska kontrolna enota rotor ponovno pospeši do zgornje frekvenčne meje 415 Hz. To frekvenčno okno je pri našem tipu SRG-merilnika fiksno in ga ne moremo spreminjati. Pri vsaki pospešitvi rotorja je ničelni premik skokovito narasel in je nato enakomerno padal, ko se je frekvenca počasi s časom zmanjševala (posledica izgub energije zaradi rezidualnega trenja).

Merjene vrednosti Ψ s **slike 2 a** lahko prikažemo na diagramu odvisnosti od frekvence (**slika 3**). V majhnem območju frekvenc med 405 Hz in 415 Hz lahko frekvenčno odvisnost aproksimiramo z linearno funkcijo.

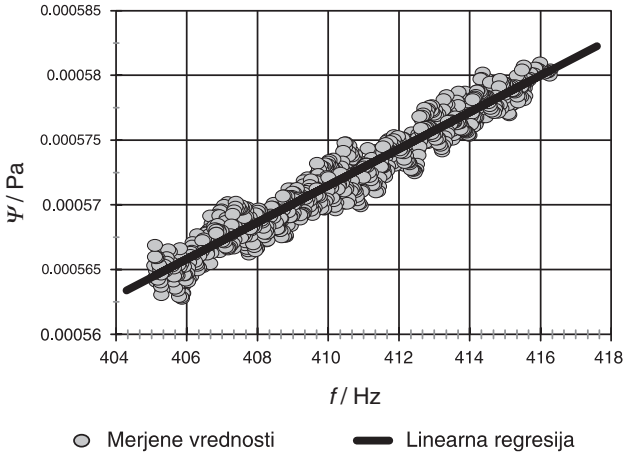

Slika 3: Prikazana vrednost SRG-merilnika (Ψ) s **slike 2** v odvisnosti od frekvence rotorja (f)

Figure 3: Displayed value of SRG (Ψ) from **Figure 2** versus rotor frequency (f)

Tabela 1: Rezultati linearne regresije merjenih vrednosti Ψ s **slike 2**
Table 1: Results of linear regression of measured values of Ψ from **figure 2**

Rezultati linearne regresije:	
Konstanta	$\boldsymbol{C}$ **=** $-9{,}8878\cdot10^{-6}$ **Pa**
Standardni odmik konstante	$1{,}0279\cdot10^{-6}$ Pa
R^2	0,94520
Število prostostnih stopenj	1169
Naklon premice	$\boldsymbol{k_f}$ **=** $1{,}418\cdot10^{-6}$ **Pa/Hz**
Standardni odmik naklona	$9{,}9\cdot10^{-9}$ Pa/Hz

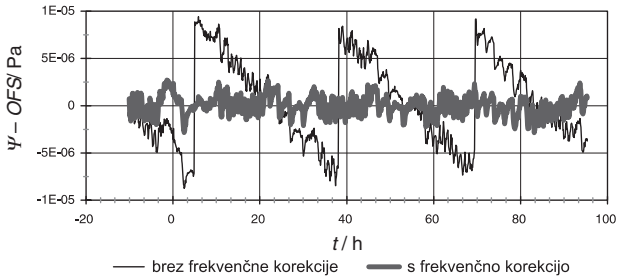

Slika 4: Merjeni signal s popravkom rezidualnega trenja (Ψ–OFS)
Figure 4: Measured signal with residual drag correction (Ψ–*OFS*) (without and with a frequency dependence)

Rezultati linearne regresije merjenih točk z metodo najmanjših kvadratov so podani v **tabeli 1**.

Popravek rezidualnega trenja v odvisnosti od frekvence lahko izračunamo iz konstante C in naklona premice k_f iz **tabele 1**:

$$OFS(f) = k_f \cdot f + C \qquad (5)$$

Razlika merjenih vrednosti Ψ in linearne aproksimacije popravka $OFS(f)$ je prikazana na **sliki 4**. Preostale variacije merjenega signala z upoštevanim popravkom rezidualnega trenja so posledica nihanj temperature ter vibracij in drugih vplivov [13]. Ker je bil tlak v sistemu manjši od $2\cdot10^{-7}$ Pa nam **slika 4** prikazuje dolgoročno stabilnost popravka rezidualnega trenja. Že na prvi pogled se zdi, da se povprečna vrednost razlike $\Psi - OFS(f)$ v času meritve ni bistveno spremenila, vendar pa je kvantitativna ocena "na pogled" zaradi znatnega raztrosa praktično nemogoča. Ker imamo na razpolago veliko število merjenih točk, si lahko pomagamo s statističnimi metodami in tudi v tem primeru kot merilo za dolgoročno stabilnost rezidualnega trenja vzamemo naklon premice, ki jo določimo z metodo najmanjših kvadratov. Naklon premice na **sliki 4** je $-3\cdot10^{-8}$ Pa/d s standardno negotovostjo $7\cdot10^{-8}$ Pa/d. To pomeni, da je izračunani naklon bistveno manjši od standardne negotovosti in lahko rečemo, da je bila vrednost rezidualnega trenja z upoštevanim frekvenčnim popravkom časovno neodvisna.

Tabela 2: Rezidualno trenje (*OFS*) pri 410 Hz in frekvenčna odvisnost (k_f) za dva SRG-rotorja pri različnih namestitvah v magnetnem ležaju. Pri obeh rotorjih sta bili uporabljeni ista kontrolna enota in merilna glava.
Table 2: Residual drag (*OFS*) at 410 Hz and frequency dependence (k_f) for different suspensions of two SRG rotors. (The same suspension head and SRG controller has been used for both rotors).

	OFS (410 Hz)	k_f
Rotor A	$5.715\cdot10^{-4}$	$1.42\cdot10^{-6}$
	$4.339\cdot10^{-4}$	$1.38\cdot10^{-6}$
	$3.141\cdot10^{-4}$	$1.88\cdot10^{-6}$
	$4.207\cdot10^{-4}$	$1.80\cdot10^{-6}$
	$4.302\cdot10^{-4}$	$2.11\cdot10^{-6}$
	$5.327\cdot10^{-4}$	$1.95\cdot10^{-6}$
Rotor B	$3.597\cdot10^{-4}$	$5.95\cdot10^{-8}$
	$2.930\cdot10^{-4}$	$3.67\cdot10^{-7}$
	$4.901\cdot10^{-4}$	$7.17\cdot10^{-7}$
	$4.081\cdot10^{-4}$	$4.52\cdot10^{-7}$
	$3.398\cdot10^{-4}$	$7.16\cdot10^{-7}$

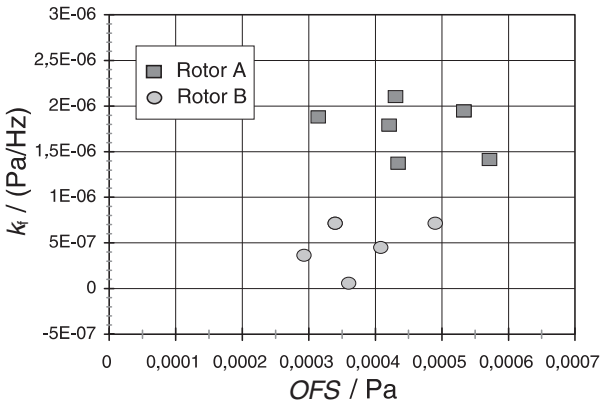

Slika 5: Ponovljivost rezidualnega trenja (*OFS*) in njegove frekvenčne odvisnosti (k_f) pri različnih namestitvah rotorja
Figure 5: Repeatability of residual drag (*OFS*) and frequency dependence (k_f) for different suspensions of the rotor

B – Ponovljivosti rezidualnega trenja za različne namestitve rotorja

Eksperiment smo nadaljevali tako, da smo rotor zaustavili, odstranili merilno glavo in jo ponovno namestili na merilno cevko. Pri tem smo dobili novo orientacijo rotorja v magnetnem ležaju glede na os vrtenja. Postopek smo večkrat ponovili in za vsako novo namestitev določili frekvenčno odvisnost rezidualnega trenja.

Neodvisno od opisanega eksperimenta smo pridobili podatke o frekvenčni odvisnosti rezidualnega trenja še za drug SRG-rotor v drugi merilni cevki, a z isto merilno glavo in kontrolno enoto. Rezultati za oba rotorja so podani v **tabeli 2** in na **sliki 5**.

Glede na razmeroma majhno število ponovitev meritve lahko rečemo, da se vrednost ofseta pri 410 Hz bistveno ne razlikuje za rotorja A in B. Pri obeh rotorjih je bila vrednost rezidualnega trenja med $3\cdot10^{-4}$ Pa in $6\cdot10^{-4}$ Pa. Opazna pa je razlika v koeficientu frekvenčne odvisnosti k_f, ki je pri rotorju A bistveno večja. Pri rotorju B smo pri eni namestitvi izmerili rezidualno trenje, ki je bilo praktično brez frekvenčne odvisnosti. V vseh drugih primerih pa je bila frekvenčna odvisnost znatna, tako da je bila pri pospešitvi rotorja od 405 Hz

do 415 Hz sprememba rezidualnega trenja med $3{,}7 \cdot 10^{-6}$ Pa in $2{,}1 \cdot 10^{-5}$ Pa, kar ima znaten vpliv pri meritvah tlaka v področju pod $1 \cdot 10^{-3}$ Pa.

5 SKLEPI

Rezidualno trenje SRG-rotorja je odvisno od frekvence vrtenja. Le včasih je frekvenčna odvisnost tako majhna, da jo lahko zanemarimo. Podobno kot velikosti rezidualnega trenja tudi frekvenčne odvisnosti ne moremo napovedati. Pri vsaki prekinitvi magnetnega lebdenja in ponovni namestitvi rotorja se naključno spremenita tako velikost rezidualnega trenja kot tudi frekvenčna odvisnost. Med njima ni zadostne korelacije, da bi lahko že iz velikosti rezidualnega trenja napovedali frekvenčno odvisnost. Poudariti pa velja, da navadno obe vrednosti ostaneta konstantni med neprekinjenim lebdenjem, tudi po večkratni pospešitvi rotorja, tako da lahko zanesljivo izračunamo popravke rezidualnega trenja pri meritvah tlaka.

6 REFERENCES

[1] J. K. Fremerey, J. Vac. Sci. Technol. A3, (**1985**),, 1715

[2] S. Dittmann, B. E. Lindenau, C. R. Tilford, J. Vac. Sci. Technol. A7, (**1989**), 3356

[3] J. K. Fremerey, Vacuum, 32, (**1982**), 685

[4] G. Comsa, J. K. Fremerey, B. Lindenau, G. Messer, P. Röhl, J. Vac. Sci. Technol. 17, (**1980**), 642

[5] B. Erjavec, J. Šetina, L. Irmančnik-Belič, Mater. tehnol., 35, (**2001**), 143

[6] J Šetina, B. Erjavec, L. Irmančnik-Belič, Mater. tehnol., 35, (**2001**), 321

[7] J. Šetina, R. Zavašnik, V. Nemanič, J. Vac. Sci. Technol. A5, (**1987**), 2650

[8] V. Nemanič, J. Šetina, J. Vac. Sci. Technol. A17, (**1999**), 1040

[9] B. Erjavec, *Vacuum*, 64, (**2001**), 15

[10] SRG 2CE, Instruction Manual, MKS Instruments, ZDA

[11] J. K. Fremerey, Rev.Sci.Instrum. 43, (**1972**), 1413

[12] C. Suk-Ho, S. Dittmann, C. R. Tilford, J. Vac. Sci. Technol. A8, (**1990**), 4079

[13] T. Bock, K. Jousten, Vacuum, 81, (**2006**), 234

UDC/UDK 621.643:620.179
Professional article/Strokovni članek

ISSN 1580-2949
MTAEC9, 41(3)151(2007)

A WET-STEAM PIPELINE FRACTURE

PRELOM CEVOVODA ZA VLAŽNO PARO

Roman Celin, Dimitrij Kmetič

Institute of Metals and Technology, Lepi pot 11, 1000 Ljubljana, Slovenia
roman.celin@imt.si

Prejem rokopisa – received: 2007-02-02; sprejem za objavo – accepted for publication: 2007-02-21

The operational reliability of a system determines the system's availability and costs during its lifetime. Taking care of the reliability usually starts with knowledge of the operating conditions that need to be considered during the design, fabrication and maintenance of the system. In the case of a system or component failure, it is necessary to know the causes and the degradation mechanisms. An analysis of a fractured low-pressure wet-steam pipeline from a heat exchanger was performed. The fracture was located in the fillet weld's heat-affected zone. Visual testing, chemical analysis, hardness measurements and metallographic examinations were carried out. The fracture surface was quite damaged, and so the number of fatigue-crack propagation cycles could not be determined. An examination of the microstructure revealed that the fatigue crack occurred in the heat-affected zone, where the plasticity and toughness had been diminished due to the material overheating at the welding. As a result of the fracture analysis the industrial facility concerned extended the scope of its inspection of wet-steam pipelines.

Key words: pipeline, fracture, examination, fatigue failure

Zanesljivost obratovanja je lastnost sistemov ali komponent, ki določa njihovo razpoložljivost in stroške v trajnostni dobi. Skrb za zanesljivost je tudi poznanje pogojev obratovanja, ki jih je treba upoštevati med konstruiranjem, izdelavo in uporabo sistema. Pri okvari sistema ali komponente pa je treba natančno poznati vzroke in mehanizme degradacije. Zaradi tega je bila opravljena analiza preloma nizkotlačnega cevovoda za vlažno paro izmenjevalnika toplote. Prelom je nastal v toplotno vplivani coni zvarjenega spoja. Izvedena je bila vizualna kontrola, kemijska analiza, meritve trdote in metalografska preiskava. Površina celega preloma je bila precej poškodovana, zato na njej ni bilo mogoče ugotoviti v koliko korakih je nastala utrujenostna razpoka. Preiskava mikrostrukture je odkrila, da se je prelom cevi izvršil v območju, kjer je bila plastičnost, z njo pa tudi žilavost, zmanjšana zaradi spremembe mikrostrukture pri varjenju zaradi pregretja materiala. Na osnovi rezultatov analize preloma je bil v industrijskem obratu povečan obseg kontrole cevovodov za mokro paro.

Ključne besede: cevovod, prelom, preiskave, utrujenostni prelom

1 INTRODUCTION

Reliability is defined as the probability that a certain system will operate for a given time and under given conditions without failure. Therefore, if a failure occurs it is wise to analyse the system and determine the probable cause of the failure[1]. In the case of metals, one of the most commons reasons for failure is fatigue. Fatigue failure is the phenomenon leading to fracture under repeated or fluctuating stresses that are less than the tensile strength of the material. There are three stages of fatigue failure: initiation, crack propagation, and final fracture[2]. The initiation site is always very small, never extending for more than the size of a few grains around the origin. The point of initiation is located at a stress concentration and this stage may be extremely small, and so difficult to distinguish from the succeeding stages of propagation and crack growth. However, after the original crack is formed, it becomes an extremely sharp stress concentration that drives the crack even deeper into the metal with each stress cycle. Whenever there is an interruption in the propagation of a fatigue fracture, characteristic marks or ridges may be observed.[3] As the propagation of the fatigue crack continues, gradually reducing the cross-sectional area, it eventually weakens the material so much that final, complete fracture occurs.

After 25 years in operation a failure occurred in a low-pressure wet-steam pipeline. This failure was not a catastrophic one, but it was severe enough to halt the operation of the system. **Figure 1** shows a sketch of the pipeline and the position of the fracture. In this case the fracture occurred in the heat-affected zone of the flange's fillet weld.

The dimensions of the tube were ϕ 60 mm × 4.8 mm. No other data were available about the tube material or the welding procedure used.

2 EXAMINATION

The fractured part of the pipeline was cut away from the broken tube and the flanges. There are a number of

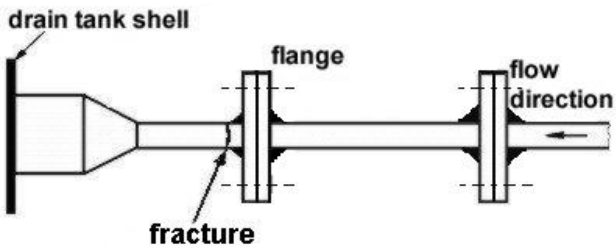

Figure 1: Sketch of the wet-steam pipeline with the fracture
Slika 1: Skica cevovoda mokre pare z mestom preloma

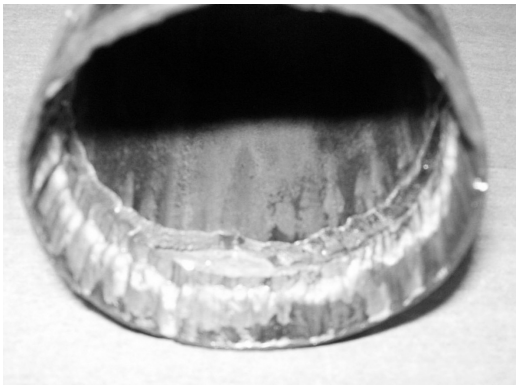

Figure 2: Tube with fracture and erosion-corrosion damage
Slika 2: Cev s prelomom in poškodbami zaradi erozije – korozije

methods available for the detection and analysis of fatigue cracks[4]. In this case it was decided to carry out a careful visual examination, a chemical analysis, hardness measurements and a metallographic examination.

3 RESULTS AND DISCUSSION

3.1 Visual examination

A visual examination of the inside area of the fractured tube revealed a substantial loss of metal, which is shown in **Figure 2.** The minimum thickness of the tube was 3 mm. The affected area was smooth with wavelike countours[5]. The minimum distance between the affected area and the fracture was of 6 mm. Flanges are not shown on **Figure 2**, becouse they were cut off.

The metal loss is oriented along the direction of the wet steam's flow and it is a classic feature of erosion-corrosion, which can be defined as the accelerated degradation of a material resulting from the joint action of erosion and corrosion when the material is exposed to rapidly moving droplets of water in a steam flow[6].

Figure 3 shows the tube's fracture surface. One area of the initial crack is marked with the number 1, and it is

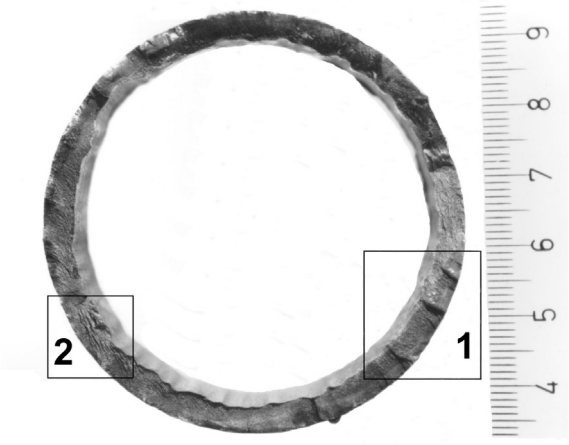

Figure 3: Tube fracture surface
Slika 3: Površina preloma cevi

Figure 4: Fatigue crack surface
Slika 4: Površina utrujenostne razpoke

shown in more detail in **Figure 4**. It is clear that the initial crack propagated in the circumferential direction more quickly than in the radial direction.

The microstructure in the initial and fatigue-crack propagation area is typical for an overheated steel. In the area subject to the highest temperature the microstructure consists of a mesh of ferrite around large grains of pearlite with many Widmanstätten ferrite needles. Such a microstructure has a low deformability and a low toughness and as such has a low fatigue strength.

Ridges are visible on the fracture surface marked with the number 2 in **Figure 3**. The details are shown in **Figure 5**.

The ridges are parallel with the tube's circumference. This kind of surface morphology is typical of rapid crack propagation in steel without significal deformation. A cross-section of the tube was cut and prepared for

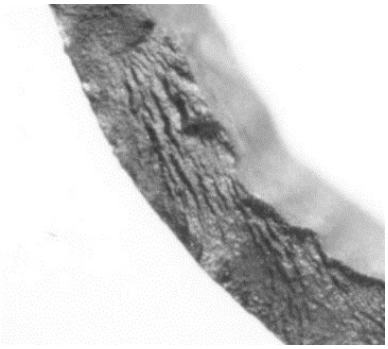

Figure 5: Ridges on the fracture surface
Slika 5: Brazde na površini preloma

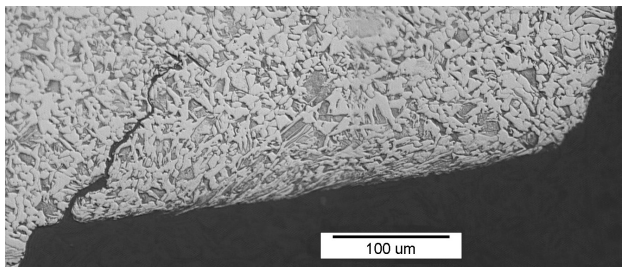

Figure 6: Crack on the fracture surface
Slika 6: Razpoka na površini preloma

metallographic examination. The crack in **Figure 6** shows transcrystal propagation typical for fatigue.

3.2 Chemical analysis

The chemical analysis of the tube material was made with an ICP optical emission spectrometer[7]. This chemical composition is listed in **Table 1**.

Table 1: Chemical composition of the tube in mass fractions, *w*/%
Tabela 1: Kemijska sestava cevi v masnih deležih, *w*/%

C	Mn	Si	P	S	Cr	Ni	Mo	Al
0.21	0.74	0.17	0.003	0.017	0.04	0.01	0.02	0.012

A comparison of the values in **Table 1** with the reference data[8] shows that the chemical composition of the tube corresponds to the steel grade ASTM A 106 Gr. B, which is widely used for the manufacturing of tubes.

3.3 Hardness measurement

A sample of the fillet weld was prepared for hardness *HV* 0.3 measurements. The results are shown in **Table 2**. The hardness indentations were 0.1 mm apart, starting in the base metal, continuing across the heat-affected zone (HAZ) and on into the weld deposit metal.

Table 2: Hardness *HV* 0.3 across the fillet weld
Tabela 2: Rezultati meritev trdot *HV* 0,3

base metal													
1.	138	2.	142	3.	141	4.	141	5.	139	6.	141		
heat-affected zone													
7.	153	8.	145	9.	145	10.	152	11.	154	12.	156	13.	163
14.	162	15.	175	16.	165	17.	174	18.	165	19.	159	20.	162
21.	178	22.	176	23.	175	24.	171	25.	177	26.	178	27.	177
28.	173	29.	194	30.	199	31.	192	32.	199	33.	196	34.	199
35.	203	36.	201										
weld deposit metal													
37.	214	38.	211	39.	210	40.	212	41.	214	42.	218	43.	217
44.	213	45.	210	46.	215	47.	211						

The average base metal hardness is *HV* 140.3; and it is within the standard values for A 106 Gr. B steel. The highest values measured were not in the HAZ, as would be expected, but in the weld deposit metal. The average value was *HV* 213, which should be considered as being relatively high.

3.4 Metallographic examination of the fillet weld

The fillet weld between the tube and the flange, with the base metal and the HAZ, is shown in **Figure 7**.

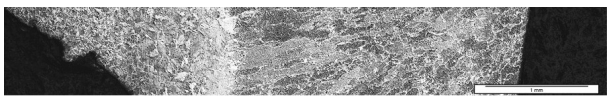

Figure 7: Fillet weld with heat-affected zone
Slika 7: Kotni zvar s toplotno vplivanim področjem

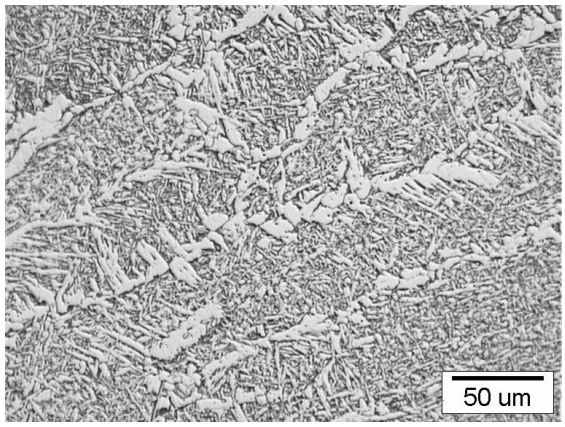

Figure 8: Microstructure of the fillet-weld deposit material
Slika 8: Mikrostruktura deponiranega materiala zvara

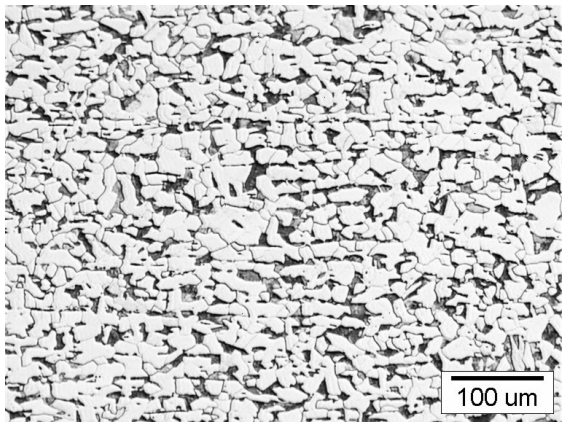

Figure 9: Microstructure of the tube's base metal
Slika 9: Mikrostruktura osnovnega materiala cevi

There is clear evidence of columnar crystals in the weld deposit metal. The microstructure consists of bainite with a small amount of ferrite in the grain boundaries after the transformation (**Figure 8**). The grains of austenite in the HAZ near the fusion line grew in size because of the overheating.

At the cooling cooling the austenite transformed into pearlite, bainite and a ferrite net. The microstructure of the base metal (**Figure 9**) consist of uniform grains of ferrite and pearlite. The wide HAZ indicates a very large input of heat during the welding.

4 CONCLUSION

After our examinations we can conclude that the fracture occurred in an area where plasticity and toughness were diminished with the overheating during the welding. The fracture took place in two stages. In the first stage a fatigue crack started to grow from one point on the outer tube surface. The propagation of this fatigue crack was much faster in the circumferential direction than in the radial direction. During the second stage the crack propagated even faster, this time without any plastic deformation. The fracture surface was damaged,

and so it is impossible to determine how many steps it took for the fatigue crack to start and how many steps it took for the final fracture to take place. Based on available data we can conclude that the main cause of the fracture was a local increase in the bending stresses on the outer tube surface because of uncontrolled, possibly resonant, vibrations of the wet-steam pipeline during the start up or the shut down of the system.

5 REFERENCES

[1] D. J. Smith, Reliability, maintability and risk, 6th ed., Butterworth Heinemann, Oxford 2001, 1–29

[2] R. E. Smallman, R. J. Bishop, Modern physical metallurgy and materials engineering, 6th ed., Butterworth Heinemann, Oxford 1999, 256–258

[3] F. Vodopivec, Kovine in zlitine, IMT, Ljubljana 2002, 121

[4] B. Kosec, G. Kovačič, L. Kosec, Engineering Failure analysis, 9 (**2002**), 603–609

[5] H. M. Herro, The Nalco guide to cooling water system failure analysis, McGraw-Hill, New York 1993, 239–250

[6] L. L. Shrerir, R. A. Jarman, G. T. Burstein, Corrosion Vol. 1, 3rd ed., Butterworth Heinemann, Oxford 2000, 294–302

[7] ASTM E 415 - 99a Standard Test Method for Optical Emission Vacuum Spectrometric Analysis of Carbon and Low Alloy Steel

[8] C. W. Wegst, Stalschlussel, Verlag Stalschlussel Wengst GmbH, 1995